Atmos. Chem. Phys., 25, 10267–10292, 2025
https://doi.org/10.5194/acp-25-10267-2025

Atmospheric Chemistry and Physics
Open Access
EGU

Gas–particle partitioning of *m*-xylene and naphthalene oxidation products: temperature and NO_x influence

Marwa Shahin, Julien Kammer, Brice Temime-Roussel, and Barbara D'Anna

Aix-Marseille Univ., CNRS, LCE, Marseille, France

Correspondence: Marwa Shahin (marwa.shahin@etu.univ-amu.fr) and Barbara D'Anna (barbara.danna@univ-amu.fr)

Received: 24 February 2025 – Discussion started: 28 February 2025
Revised: 28 May 2025 – Accepted: 12 June 2025 – Published: 10 September 2025

Abstract. Volatile organic compounds (VOCs) react with atmospheric oxidants, resulting in oxygenated products of lower volatility known as semi-volatile and intermediate-volatility organic compounds (S/IVOCs), which form secondary organic aerosols (SOAs). Those compounds can partition between the gas and particle phases, a critical process that is influenced by several environmental parameters yet is poorly constrained. This study aims to evaluate the effect of temperature and the VOC/NO_x ratio on SOA formation and the partitioning of individual SOA products from *m*-xylene and naphthalene OH oxidation. Experiments are carried out in an oxidation flow reactor (OFR), and products are identified and quantified using a proton transfer reaction time-of-flight mass spectrometer (PTR-ToF-MS) coupled to a CHemical Analysis of aeRosol ONline (CHARON) inlet. Results show that lower temperatures significantly enhance SOA formation, while lower VOC/NO_x ratios reduce it. Gas-phase *m*-xylene major products are C_3, C_5, and C_8 compounds, whereas particle–product distributions exhibit a progressive increase from C_2 to C_8. In contrast, naphthalene products partition more readily into the condensed phase, with C_8–C_{10} products dominating. Most of the oxidation products from both precursors exhibit a volatility distribution in the SVOC regime, with fewer in the IVOC regime. The decrease in temperature shifts the effective saturation concentration (C_i^*) values towards lower values, although no clear relationship between C_i^* and the oxidation state is observed. A comparison between observed and estimated volatilities using a model based on the group contribution method (SIMPOL.1) reveals systematic deviations for both light molecules and heavy compounds, suggesting a need for improved predictive models.

1 Introduction

Aromatic hydrocarbons (AHs) are a ubiquitous class of air pollutants and contribute an important fraction to the total of volatile organic compounds (VOCs) in urban environments; the relative contribution may vary and depends on the location and season (Calvert et al., 2002; Jiang et al., 2017; Montero-Montoya et al., 2018). Among the different AHs, xylene and naphthalene are important anthropogenic VOCs that are primarily emitted by petrochemical industries, biomass burning, diesel and gasoline engines, or solvent evaporation (Fang et al., 2021, 2024; Wu et al., 2020; Xuan et al., 2021). In the atmosphere, AHs react with common oxidants such as hydroxyl (OH), nitrate (NO_3), and chloride (Cl) radicals and ozone (O_3), leading to the formation of oxygenated reaction products of lower vapor pressures, also known as semi-volatile organic compounds (SVOCs) and intermediate-volatility organic compounds (IVOCs) (Seinfeld and Pandis, 2016). These compounds may partition into the particle phase, forming secondary organic aerosols (SOAs) that represent approximately 60 % of ambient organic aerosol (Huang et al., 2020, 2014) and have an impact on visibility (Li et al., 2014; Liu et al., 2017), climate (Liu and Matsui, 2020; Shrivastava et al., 2017), and human health (Anderson et al., 2012; Berlinger et al., 2024; Singh and Tripathi, 2021; Thangavel et al., 2022). Indeed, particulate air pollution is closely correlated with the progression of numerous respiratory diseases in addition to cancer, cardiovascular diseases, and neurological damage (Liu et al., 2022a; Singh

and Tripathi, 2021; Song et al., 2017; Thangavel et al., 2022). Each year in the EU, around 238 000 premature deaths are attributable to fine particulate matter ($PM_{2.5}$) exposure (European Environment Agency, 2022). Improving our understanding of particle sources and properties is thus crucial to the creation of a more sustainable environment.

Over the last decades, many laboratory and modeling studies have investigated the SOAs generated by AH reaction products (Chen et al., 2018; Forstner et al., 1997; Klodt et al., 2023; Lannuque et al., 2018; Li et al., 2022; Liu et al., 2023, 2022b; Lu et al., 2024a; Song et al., 2007; Srivastava et al., 2022; Tian et al., 2023). The OH radical oxidation of monoaromatic compounds operates through two main pathways (Atkinson et al., 1991; Bloss et al., 2005; Calvert et al., 2002; Forstner et al., 1997; Pan and Wang, 2014). In the case of *m*-xylene, the first pathway is OH radical addition to the aromatic ring, predominantly in the ortho position (Fan and Zhang, 2008) to form a hydroxy-methyl-benzyl radical with the subsequent addition of O_2 to form a bicyclic radical, a major ring-opening product channel (Zhao et al., 2005). The second reaction pathway is H abstraction from the methyl group to form a methyl benzyl radical, with the subsequent addition of O_2 to form a benzyl peroxy radical (Atkinson et al., 1991; Molina et al., 1999). In the presence of NO_x, the peroxy radical mainly reacts with NO to form an alkoxy radical, and finally abstraction by O_2 leads to the formation of *m*-tolualdehyde (Srivastava et al., 2023). In the case of naphthalene, the OH radical reaction is initiated exclusively by OH addition, most predominantly at the α -carbon (68 %) adjacent to the fusion of naphthalene's two aromatic rings (Wang et al., 2007). Then, a hydroxy cyclohexadienyl radical is formed, which further reacts with NO_2 to form nitrogen-containing compounds or with O_2 to form various products, out of which 2-formyl cinnamaldehyde is the major product (Nishino et al., 2009).

The NO_x level has been shown to have significant yet possibly contrasting effects on SOA formation (Chan et al., 2009; Liu et al., 2024; Ng et al., 2007; Qi et al., 2020; Sarrafzadeh et al., 2016; Song et al., 2005; Zhu et al., 2021). Some studies have reported a decrease in SOA yield under high-NO_x conditions, which can be explained by the termination reactions of NO with the peroxy (RO_2 and HO_2) and OH radicals, limiting the formation of lower-volatility compounds (Chan et al., 2009; Ng et al., 2007; Song et al., 2005). Nonetheless, Zhu et al. (2021) reported an increase in SOA mass under elevated levels of NO_x compared to in NO_x-free experiments. Enhanced SOA formation under high NO_x has also been linked to the formation of organic nitrates and the isomerization of alkoxy radicals into low-volatility products, or it is related to a change in OH concentration due to the presence of NO_x (Ng et al., 2007; Schwantes et al., 2019; Shi et al., 2022; Srivastava et al., 2023). Under low-NO_x conditions, RO_2 radicals primarily react with HO_2 to form low-volatility organic hydroperoxides, which contribute to new-particle formation and increase SOA mass (Xu et al., 2014; Zhao et al., 2018). These findings illustrate that NO_x is capable of both inhibiting and promoting SOA formation depending on the NO_x regime.

A key process determining the fate of the oxidation products generated from AH oxidation is their ability to partition between the gas and particle phases, either throughout nucleation, forming new particles, or by condensing on pre-existing particles. Partitioning is influenced by many environmental parameters such as temperature, relative humidity, the nature and the diameter of the pre-existing particles on which they condense, and the physio-chemical properties of the S/IVOC condensing (Kamens et al., 2011; Kim et al., 2007; Lannuque et al., 2018; Loza et al., 2012; Ng et al., 2007; Qi et al., 2010; Sato et al., 2007; Takekawa et al., 2003; Warren et al., 2009; Xu et al., 2015).

SOA yields increase at lower temperatures, a well-known trend that is consistently reported for both terpenes and isoprene (Clark et al., 2016; Deng et al., 2021; Svendby et al., 2008; Virtanen et al., 2010), aromatics (Lannuque et al., 2023; Svendby et al., 2008), alkanes (*n*-dodecane in Fan et al., 2025; Li et al., 2020), and amines (Price et al., 2016). This behavior is attributed primarily to the decrease in the vapor pressures of the compounds, displacing the equilibrium towards the particle phase. However, the impact of temperature on SOA composition is not fully understood and seems to depend on other experimental conditions (precursor, seed acidity, etc.). For biogenic precursors, previous studies reported more oligomer formation at lower temperatures (Li et al., 2020; Fan et al., 2025), driven by increased SVOC partitioning and condensed-phase reactions, while others observed the opposite, attributing higher-temperature oligomerization to radical- or acid-catalyzed reactions (Clark et al., 2016; Deng et al., 2021; Price et al., 2016). Additionally, Li et al. (2019) highlighted how lower temperatures increase SOA viscosity, suppressing evaporation and favoring the retention of low-volatility species. Conversely, Lamkaddam et al. (2017) found a weak temperature sensitivity in SOA formation from *n*-dodecane, suggesting that extremely low-volatility products and compensating shifts in product types may offset volatility effects. Regarding aromatic compounds, only Lannuque et al. (2023) investigated the effect of temperature on SOA chemical composition at the molecular level, showing the general agreement of product distributions between 280 and 295 K. Thus, more studies on different aromatic precursors and experimental conditions are needed to complete our understanding of the temperature effect on SOA formation from aromatic precursors.

Although temperature is recognized as a major factor governing gas–particle partitioning, most prior studies have mostly focused on the bulk SOA yields or on selected classes of compounds (Ahn et al., 2021; Bahrami et al., 2024; John et al., 2018; Rutter and Schauer, 2007; Svendby et al., 2008; Takekawa et al., 2003; Wei et al., 2016; Zhang et al., 2023; Zhou, 2021). While these approaches have advanced the understanding of SOA formation and representation in mod-

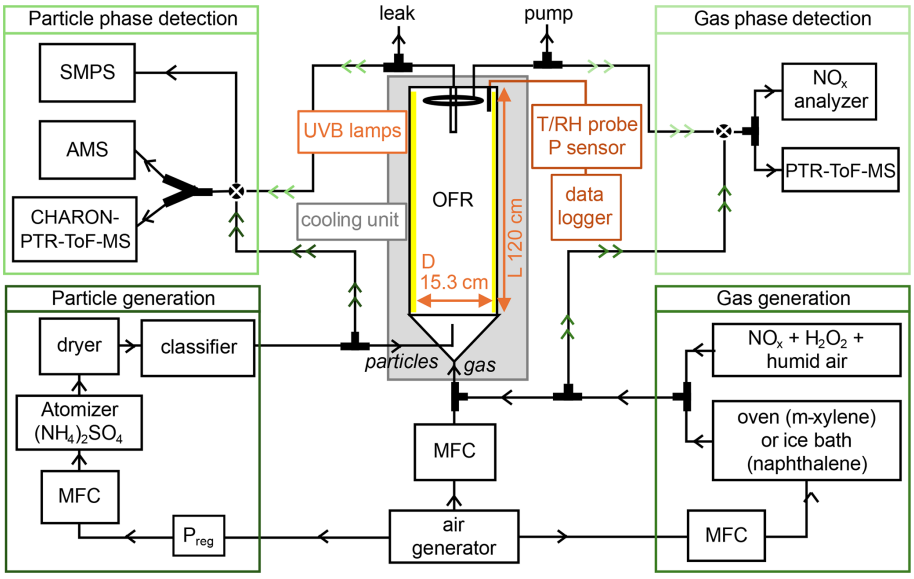

Figure 1. Schematic of the experimental setup. MFC stands for mass flow controller.

els, they often lack molecular-level-resolved resolution. Experimental studies that probe the effects of temperature on the partitioning of individual SOA oxidation products remain limited and relatively recent (Deng et al., 2021; Fan et al., 2025; Lannuque et al., 2023; Li et al., 2024). Such measurements are particularly important for refining SOA volatility parameterizations under atmospherically relevant cold conditions, such as those occurring during nighttime or wintertime episodes.

The oxidation flow reactor (OFR; Fig. 1) is a type of continuous-flow reactor that uses substantially elevated oxidant levels to rapidly simulate atmospheric oxidation chemistry (Kang et al., 2007; Peng and Jimenez, 2020). Lannuque et al. (2023) have studied the gas–particle partitioning of toluene in a similar OFR system. Experiments carried out at 280 K were characterized by higher mass loading in the particle phase compared to those at 295 K, as well as by a shift in volatility values of oxidation products towards lower volatility values.

Direct measurements of S/IVOCs in real time remains challenging due to their complexity, diversity, and low concentrations. The analytical development of the CHemical Analysis of aeRosol ONline (CHARON) inlet coupled with a proton transfer reaction time-of-flight mass spectrometer (PTR-ToF-MS) enables alternative online measurements of both gas and particle phases at the molecular level (Eichler et al., 2015). It also allows us to measure both gas and particle phases, with reduced artifacts associated with particle collection and thermal desorption compared to traditional techniques (Peng et al., 2023). Promising applications have been shown in several laboratory and field studies (Lannuque et al., 2023; Müller et al., 2017; Müller et al., 2017; Piel et al., 2021), but its application to gas–particle partitioning investigations is relatively new (Gkatzelis et al., 2018; Lannuque et al., 2023; Peng et al., 2023; Piel et al., 2021).

The aim of the present study is to evaluate gas–particle partitioning of the S/IVOCs involved in SOA formation from the photooxidation of AHs under different conditions. For that purpose, the photooxidation of AH compounds was investigated using an online CHARON-PTR-ToF-MS coupled to an oxidation flow reactor. These laboratory experiments aim to (1) identify the gas- and particle-phase products of *m*-xylene and naphthalene at a molecular level, (2) evaluate the partitioning behavior of individual SOA products, and (3) assess the effect of atmospheric conditions (temperature variation and the NO_x/VOC ratio) on this partitioning. Two compounds, *m*-xylene and naphthalene, are selected for the following reasons: (i) their ubiquity in urban areas (Fang et al., 2021; Wu et al., 2020; Xuan et al., 2021); (ii) their known reactivity with OH radicals, which is on the same order of magnitude (Calvert et al., 2015); and (iii) their SOA formation potential, which has been previously demonstrated (Chan et al., 2009; Chen et al., 2016, 2021; Kleindienst et al., 2012; Li et al., 2022; Loza et al., 2012; Lu et al., 2024b; Ng et al., 2007; Sato et al., 2022; Song et al., 2005, 2007; Srivastava et al., 2022; Takekawa et al., 2003; Ye et al., 2024; Zhang et al., 2019a, b).

2 Methods

2.1 The OFR experimental setup

Photooxidation experiments were conducted in a 19.3 L cylindrical aerosol oxidation flow reactor (OFR; 153 mm internal diameter, 105 cm length) made up of quartz, which is vertically oriented and surrounded by six UVB lamps (He-

lios Italquartz) with a continuous emission spectrum in the 280–350 nm range ($\lambda_{max} = 310$ nm, Fig. 1). An external air conditioning unit is connected to the tube, allowing temperature control in the range of 280–295 K. The gas-phase stream consists of humid air, the selected VOC precursor (*m*-xylene or naphthalene), nitrogen dioxide (NO_2), and hydrogen peroxide (H_2O_2). For humidification, two glass bottles containing Milli-Q water are bubbled at 0.2–1 L min^{-1} with pure N_2 in order to maintain relative humidity (RH) around 50 % (from 35 % to 65 % among all experiments). A constant concentration of *m*-xylene is generated using a constant flow of 0.15 L min^{-1} of N_2 over a permeation tube containing a pure solution ($\geq$ 99 % purity, Sigma Aldrich) placed in an oven and kept at a constant temperature of 308 K. Some solid naphthalene (99 % purity, Sigma Aldrich) is kept in an ice water bath, while headspace is maintained at 0.1 L min^{-1} using pure N_2 to generate a constant flow of naphthalene in the flow tube. NO_2 is introduced using a cylinder (100 ± 5 ppm of N_2, Linde) and is diluted to the desired mixing ratios with N_2 using different mass flow controllers prior to entering the OFR (varying from 40 to 340 ppbv) depending on the required VOC/NO_x conditions. A hydrogen peroxide (H_2O_2) solution (50 % H_2O, stabilized, Sigma Aldrich) is used as a hydroxyl radical (OH) precursor and is constantly introduced into the OFR by bubbling pure N_2 into the solution at a flow of 0.1–0.2 L min^{-1}. For each experiment, the OH radical concentration generated was estimated by fitting the VOC precursor (*m*-xylene or naphthalene) decay, assuming a pseudo-first-order reaction with OH radicals using temperature-dependent values of the kinetic rate constant recommended by the NIST kinetics database. This estimation is also based on the hypothesis that the other reactions with OH do not limit the reaction of the precursor in the first seconds following the lamps switching on. The OH radical concentrations range from 2.2 to 5.4×10^7 molecules cm^{-3}, corresponding approximately to 1.3 and 3 d of atmospheric OH radical exposure, taking into account a diurnal average hydroxyl radical concentration of 1.5×10^6 molecules cm^{-3} (Mao et al., 2009). Due to background contamination, compounds with m/z of 61 and below, mainly acetaldehyde, acetic acid, formaldehyde, and formic acid, are not considered in further analyses. Monodispersed ammonium sulfate (AS) seeds serve as a pre-existing surface and are generated by nebulizing a 10^{-2} M AS solution (99.5 % purity, Acros Organics) using an atomizer (TSI Inc., model 3076), dried with a silica diffusion drier and then size selected in an aerodynamic aerosol classifier (AAC, Cambustion) to generate monodisperse aerosols with an average diameter of 200 nm. The overall input flow is 2.4 L min^{-1} to ensure a residence time of 8 min in the tube. In this configuration, particle losses (or their transmission through the OFR) were estimated by comparing the concentrations of seed particles at the inlet and outlet of the OFR when generating seeds at 200 nm electrical mobility diameters. These losses were checked daily prior to each experiment and were in the range of 10 ± 5 %. In addition, precursor losses were estimated to be around 5 % for *m*-xylene and 10 %–15 % for naphthalene. Losses of the gaseous products generated during SOA experiments were not experimentally evaluated. Lannuque et al. (2023) showed in a toluene SOA experiment that wall losses introduced a 10 %–15 % deviation in the SOA yield when considering both precursors and reaction products. For *m*-xylene, we can reasonably assume lower losses, as the residence time is shorter and the flow tube has a larger inner diameter. For naphthalene, it is probable that the wall losses were higher than those of *m*-xylene.

2.2 Instrumentation and data analysis

Figure 1 shows the schematic of the experimental setup, where several online instruments are used to characterize gas- and particle-phase chemical compositions, as well as particle number and size distribution.

A commercial proton transfer reaction time-of-flight mass spectrometer (PTR-Tof-MS 6000X2, Ionicon Analytik GmbH, Innsbruck, Austria) coupled to a CHemical Analysis of aeRosol ONline (CHARON) inlet is used to follow the gas- and particle-phase chemical composition of the organic fraction online. The CHARON inlet has been already described in detail elsewhere (Eichler et al., 2015; Leglise et al., 2019; Müller et al., 2017). Briefly, the sampled air travels through three major sections of the CHARON inlet: (1) a gas-phase denuder of activated charcoal that strips off gaseous organics, (2) an aerodynamic lens system (ADL) that collimates the subsampled flow and subsequently enriches the particle concentration, and (3) a thermodesorption unit (TD) heated at $T = 150$ °C that vaporizes the particles prior to their introduction into the drift tube. The PTR-ToF-MS is used with hydronium ions (H_3O^+) to ionize organic analytes and operates at a drift tube pressure of 2.6 mbar, a temperature of 120 °C, and a voltage of 230 V. This results in $E/N = 68$ Td (E = electric field, N = number density of the gas molecules in the drift; 1 Td = 10^{-17} V cm^2 molecule^{-1}). It represents a relatively low E/N compared to the classical 120–140 Td reported in most PTR-ToF-MS studies, as the aim is to minimize the potential fragmentation of parent ions and facilitate the molecular characterization of SOA. The potential higher dependence of the sensitivity on relative humidity variations at such a low E/N can be neglected, as all experiments were conducted at fixed relative humidity (Pang, 2015; Tani et al., 2003).

Instrument background checks were performed daily using pure N_2, while sensitivity and particle enrichment factors (EFs) were controlled at the end of the experiments. A blank was tested prior to each SOA experiment using the same conditions (H_2O_2 flow, NO_x concentration, temperature, humidity, etc.), in the absence of the VOC precursor (either *m*-xylene or naphthalene). The products formed during these daily blanks were quantified and subtracted from the signal of the following experiment. EF is determined by CHARON

calibration using a vanillic acid solution based on the method recommended by Eichler et al. (2015). Instrument sensitivity is evaluated by calculating the transmission curve using a cylinder containing 14 gas standards (benzene; toluene; ethylbenzene; *o*-, *m*-, and *p*-xylene; styrene; 1,2,4-trimethyl- and 1,3,5-trimethylbenzene; and chloro-, 1,2-dichloro-, 1,3-dichloro-, 1,4-dichloro-, and trichlorobenzene, each at 100 ppb ±10 % of N_2; RESTEK) covering a mass range up to m/z 181.

An IDA (Ionicon data analyzer 2.1.1.4) is used to process data recorded by the PTR-ToF-MS, such as mass calibration, peak shape definition, peak identification and integration, rate constant calculation, and VOC quantification (Müller et al., 2013). The peaks at m/z 21.022 ($H_3^{18}O^+$) and m/z 330.847, corresponding to diiodobenzene ($C_6H_5I_2^+$) and its fragment at m/z 203.943 ($C_6H_5I^+$), are used to recalibrate the mass scale (PerMaSCal® internal standard, 1,3-diiodobenzene, $T = 55\,°C$). Molecular formulas composed of C, H, O, and N atoms are assigned based on the exact mass position, chemical rules (the valence of atoms, for example), and isotopic patterns. The molecular formula is used to calculate dipole moments and polarizability, as introduced by Bosque and Sales (2002) and Sekimoto et al. (2017), which allows us to calculate the k-rate constants based on ion–molecule collision theories (Gioumousis and Stevenson, 1958; Langevin, 1950; Su and Chesnavich, 1982). Concentrations are then estimated based on the rate constant between a proton and each VOC, the experimental transmission of each compound, and the primary ion intensity.

RStudio (RStudio 2023.06.0 Build 421) is used to perform a non-targeted approach for compound selection based on the stability periods before and after oxidation. Time intervals are defined for each experiment corresponding to blanks (photooxidation without VOC precursors and a HEPA (high-efficiency particulate air) filter for the particle phase), reactants (injection of products before the light is turned on), and products (stable photooxidation) for both gas and particle phases. The Welch t test is then used to statistically identify ions that are more concentrated than those in the blank. Then, among the selected ions, the products are defined as the compounds that are more concentrated during the oxidation period and the inverse for reactants, which is also based on the Welch t test.

A high-resolution time-of-flight aerosol mass spectrometer (HR-ToF-AMS, Tofwerk AG, Aerodyne Inc. USA) is employed for the quantification of the organic and inorganic aerosol fractions (Canagaratna et al., 2007; DeCarlo et al., 2006), with the data recorded by the AMS analyzed using the software SQUIRREL (ToF-AMS analysis toolkit 1.65C). The ionization efficiency (IE) with respect to nitrate anions was 4.58×10^{-8}. It was calculated using nebulized 300 nm mobility diameter ammonium nitrate particles (BFSP software). The relative IE (RIE) of ammonium was 3.45 based on the mass spectrum of ammonium nitrate data from IE calibrations. The RIE of sulfate was determined by comparing the theoretical and the measured concentrations of a solution of ammonium nitrate and ammonium sulfate, and it was determined to be 1.75. For the organic fraction, the default value of 1.4 was used. The AMS data were corrected by the collection efficiency (CE) calculated by comparison to the SMPS (scanning mobility particle sizer, TSI classifier model 3082, differential mobility analyzer (DMA), TSI condensation particle counter (CPC) 3776) volume using densities of 1.7 $g cm^{-3}$ for ammonium sulfate and 1.4 $g cm^{-3}$ for organics. The CE values varied from 0.3 for pure ammonium sulfate particles to 0.7 after SOA formation.

The SMPS is used to measure particle size distribution and number concentration. Additional instruments account for a chemiluminescent NO_x analyzer (Envitec, model API200E), a pressure sensor (ATM.ECO, STS), and a temperature–humidity probe (HMP9 Vaisala) positioned close the aerosol flow tube outlet, the last two instruments being connected to a data logger (FieldLogger, NOVUS).

2.3 SOA yield, partitioning, and volatility distribution

The expression to describe the fractional aerosol yield (Y) was established by Odum et al. (1996, 1997) and is described in Eq. (1), where ΔM_0 is the amount of the total organic aerosol formed (in $\mu g\,m^{-3}$), and ΔVOC is the amount of the VOC precursor involved in the reaction (in $\mu g\,m^{-3}$), measured as the difference between the VOC concentrations at the inlet and outlet of the OFR.

$$Y = \frac{\Delta M_0}{\Delta \mathrm{VOC}} \tag{1}$$

The distribution of oxidation products between the gas and particle phases can be explained by the partitioning theory of Yamasaki et al. (1982):

$$K_{\mathrm{p},i} = \frac{C_{\mathrm{p},i}}{C_{\mathrm{g},i} \times \mathrm{TSP}}, \tag{2}$$

where $K_{\mathrm{p},i}$ is the experimental partitioning coefficient (in $m^3\,\mu g^{-1}$) of a species i; $C_{\mathrm{p},i}$ and $C_{\mathrm{g},i}$ are concentrations (in $\mu g\,m^{-3}$) of the species i in the particle and gas phases, respectively, as measured by the CHARON-PTR-ToF-MS; and TSP is the total suspended particulate matter of the aerosol (in $\mu g\,m^{-3}$), as measured by SMPS. Larger K_{p} values indicate a preference for compound partitioning into the particle phase. Subsequently, the volatility of the species can be defined by $\log_{10} C_i^*$, where C_i^* is known as the effective saturation concentration (in $\mu g\,m^{-3}$) of a species i, which describes the gas–particle partitioning behavior of organic compounds and represents the gas-phase concentration of a compound at which it will partition equally between the gas and particle phases under given atmospheric conditions; it is calculated as the reciprocal of $K_{\mathrm{p},i}$ (Donahue et al., 2006, 2011):

$$C_i^* = \frac{1}{K_{\mathrm{p},i}}. \tag{3}$$

The estimated values have been calculated using the Volcalc model based on molecular properties such as molecular weight, numbers of atoms, and functional groups (Meredith et al., 2023; Riemer, 2023). The model is based on SIMPOL.1, a group contribution method (Pankow and Asher, 2008) that implements a structure–activity relationship method to calculate the subcooled pure-liquid vapor pressure by summing the contributions of the subcooled liquid vapor pressures of individual chemical functional groups:

$$\log_{10} P^{\circ}_{\mathrm{L},i}(T) = \sum_{k} v_{k,i} b_k(T), \quad (4)$$

where $P^{\circ}_{\mathrm{L},i}(T)$ is the liquid vapor pressure (atm), $v_{k,i}$ is the number of groups of type k in i, the index k can take any number (1, 2, 3, etc.), and $b_k(T)$ is the group contribution term for group k. No second-order interaction terms are included to account for neighboring functional groups, which means that the model does not consider the potential interactions or effects that adjacent functional groups might have on each other but only sums the contributions of individual functional groups independently.

The saturation concentration ($C^{\circ}_{i,T}$) of the major identified species i is calculated at $T = 280$ and 295 K as follows:

$$C^{\circ}_{i,T} = C^{\circ}_{i,293} \times \frac{293}{T} \times \exp\left(\left(\frac{-\Delta H}{R}\right) \times \left(\frac{1}{T} - \frac{1}{293}\right)\right), \quad (5)$$

where $C^{\circ}_{i,293}$ is the saturation concentration calculated by Volcalc at $T = 293$ K; ΔH_i is the enthalpy of vaporization of species i (computationally predicted values from ChemSpider); and R is the ideal gas constant, 8.314 J mol^{-1} K^{-1}.

The saturation concentration (C°_i) and the effective saturation concentration (C^*_i) are related through the activity coefficient (γ_i) that captures the non-ideal interactions of the compound with the aerosol mixture. Its value generally lies between 0.3 (readily partitions to particle phase) and 3 (readily partitions to gas phase) for ambient atmospheric aerosol (Donahue et al., 2011; Liu et al., 2021). As in previous studies, such as Isaacman-VanWertz et al. (2016) and Nie et al. (2022), in this work we assume a γ value of 1.

3 Results and discussion

3.1 SOA yield formation

Table 1 summarizes the experimental conditions, reactants consumed (ΔVOC), and newly formed organic aerosol mass (ΔM_0) that are used to calculate the SOA yield (Y) for each experiment (Eq. 1). Figure 2 presents SOA yields for (a) *m*-xylene and (b) naphthalene, comparing them with results from select previous studies (Chan et al., 2009; Chen et al., 2018; Ng et al., 2007; Song et al., 2005). Filled markers indicate high-NO_x conditions (VOC/NO_x < 8); empty markers refer to low-NO_x conditions (VOC/NO_x > 8) (Dodge, 1977; NARSTO and Electric Power Research Institute, 2000). The red-square and blue-triangle markers refer to this study at 295 and 280 K, respectively, while all other experiments are conducted at room temperature (between 295 and 300 K).

For *m*-xylene (Fig. 2a), the SOA yield at 295 K under high-NO_x conditions is approximately 8 % (filled red square), in line with values reported by Ng et al. (2007) and Chen et al. (2018). Chen et al. (2018) reported yields with higher VOC/NO_x ratios, with slightly lower precursor concentrations (44–59 ppb), and without using seeds. The absence of seed particles reduces the available surface area for the condensation of oxidized products (Lambe et al., 2015). Ng et al. (2007) conducted experiments with AS seeds, similar to in our study, but using nitrous acid (HONO) as the OH radical precursor, with varying initial xylene concentrations (from 42 to 171 ppb) that may explain the SOA yield variability (from 3 % to 8 %). Higher initial levels of the VOC precursor have been shown to reduce aerosol formation (and the amount of the precursor involved in the reaction) and the formation of oxidation products, especially those with $m/z > 110$ Da (Chen et al., 2019). It may be due to the competition between IVOC reactions with OH that produce low-volatility organic compounds or extremely low-volatility organic compounds (LVOC/ELVOC) and precursor oxidation. In our case, the initial *m*-xylene concentration was kept similar between experiments to isolate the effect of temperature and NO_x on SOA yield and chemistry. The studies by Ng et al. (2007) and Chen et al. (2018) were conducted under dry conditions. Li et al. (2022) reported SOA yields increasing from 6.3 % to 14 % when humidity increased from 10 % to 70 %. The order of magnitude of SOA yields in that study is close to what we observed, with the variability in yields being associated mostly with NO_x or NH_3 initial concentrations. Under low NO_x, an SOA yield of 14 % (empty red square) is observed, lying in the lower range (12 %–30 %) of the values reported by Song et al. (2007), who used lower levels of xylene (39–52 ppb).

The effect of temperature on SOA yield is also depicted in Fig. 2. When decreasing from 295 to 280 K, SOA yield increases from 8 % to 23 % under high-NO_x conditions and from 14 % to 28 % under low-NO_x conditions. Only a few studies have investigated the role of low temperature on SOA formation from monoaromatic precursors. Regarding xylene, only Takekawa et al. (2003) reported that SOA yield is enhanced by a factor of around 2 (from 6 %–13 % on average) when temperature decreases from 303 to 283 K at a VOC/NO_x ratio around 10 (similar to the low-NO_x conditions in this study). This is in good agreement with our results, where a decrease of 15 K doubles the SOA yield under low-NO_x conditions (Fig. 2). Lannuque et al. (2023) found a similar temperature dependence of toluene SOA and highlighted the finding that the effect was greater for low concentrations of the precursors.

For naphthalene (Fig. 2b), the SOA yield at 295 K with high-NO_x conditions ranges from 15 % to 18 %, in agreement with Chen et al. (2016) and Chan et al. (2009), who reported

Table 1. List of the laboratory experiments conducted and associated conditions, such as the OFR temperature, RH, VOC/NO_x ratio, seed mass, and SOA yield.

	T	RH	VOC	NO_x	VOC/NO_x	Seeds	[OH] $\times 10^7$	ΔVOC		ΔM_0	Y
	K	%	ppbv	ppb	ppb C ppb^{-1}	μg m^{-3}	molecules cm^{-3}	μg m^{-3}	%	μg m^{-3}	%
m-xylene	280 ± 1.5	75 ± 5	74 ± 0.65	235	2.5 ± 0.1	51 ± 1.6	3.4 ± 0.5	114 ± 3.3	34	26.4 ± 1.2	23.1 ± 1.2
	280 ± 1.5	50 ± 5	69 ± 0.70	40	13.9 ± 0.5	35 ± 0.5	2.2 ± 0.4	95 ± 3.3	30	26.1 ± 1.9	27.5 ± 2.1
	295 ± 2	60 ± 7	73 ± 0.66	221	2.6 ± 0.1	30 ± 0.8	5.4 ± 0.8	155 ± 3.2	49	12.6 ± 1.4	8.1 ± 1.0
	295 ± 2	55 ± 7	83 ± 0.74	40	16.6 ± 0.6	34 ± 0.7	4.7 ± 0.7	153 ± 3.2	42	21.1 ± 1.4	13.8 ± 1.0
naphthalene	280 ± 1.5	40 ± 3	57 ± 0.35	340	1.7 ± 0.1	46 ± 0.6	2.9 ± 0.2	92 ± 2.3	29	23.3 ± 1.8	25.3 ± 2.0
	280 ± 1.5	35 ± 3	53 ± 0.41	62	9.3 ± 0.4	36 ± 1.0	3.2 ± 0.3	79 ± 2.3	27	33.6 ± 6.9	42.7 ± 8.8
	295 ± 2	40 ± 5	53 ± 0.47	340	1.6 ± 0.1	55 ± 1.5	3.5 ± 0.3	84 ± 2.3	28	12.6 ± 1.7	14.9 ± 2.1
	295 ± 2	50 ± 5	49 ± 0.41	57	8.6 ± 0.4	65 ± 0.3	3.1 ± 0.4	75 ± 2.2	29	13.8 ± 1.6	18.3 ± 2.2

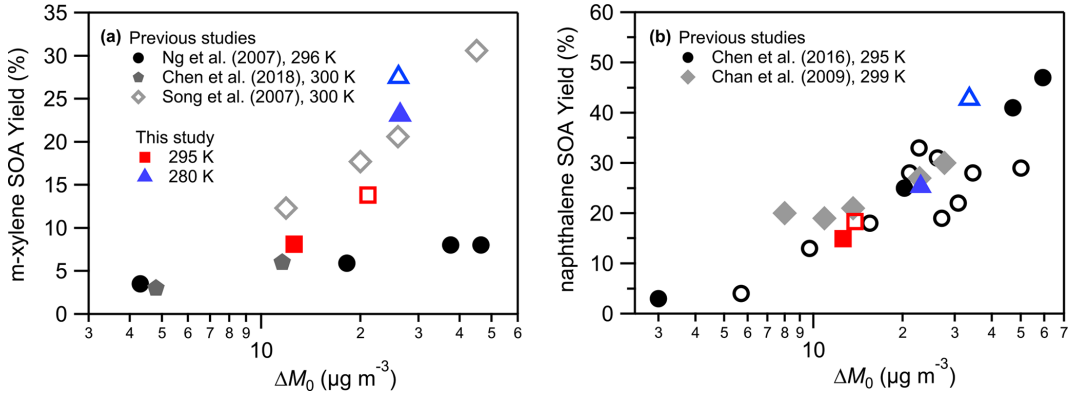

Figure 2. SOA yields at 295 and 280 K as a function of organic aerosol mass formed for **(a)** *m*-xylene and **(b)** naphthalene in comparison with previous studies. Filled markers correspond to high-NO_x conditions and open markers to low NO_x.

values from 3 % to 47 %. Chen et al. (2016) observed the lowest SOA yield under high NO_x, attributed to the lowest amount of OH generated and the highest NO injection. Even though Chan et al. (2009) used AS seeds, the initial amount of naphthalene was less than half of that used in our experiments, and the humidity was below 10 %, again highlighting the important effect of experimental conditions on the prediction of SOA yields. Lower naphthalene SOA yields are observed under high-NO_x conditions (filled vs. empty square or triangle, Fig. 2). Under low-NO_x conditions, a yield of 18 % is observed, in quite good agreement with the results of Chen et al. (2016), who reported yields varying from 4 % to 29 % as a function of the VOC/NO_x ratio, with the lowest yields for the highest-NO_x regimes. A consistent increase in SOA yield is observed when switching from the high- to the low-NO_x regime at 280 K, from 25 % to 43 % at 280 K, while at 295 K the variation is limited to an increase of a few percent. The presence of NO_x in the system may promote a competition between peroxy radicals (RO_2 and HO_2) and NO_x (NO_2 and NO) for the termination reaction of RO_2 radicals, leading to less oxidized products of higher volatility (Henze et al., 2008; Kroll and Seinfeld, 2008).

The effect of temperature on naphthalene SOA is reported here for the first time. Reducing the temperature from 295 to 280 K induces an increase from 14.9 % to 25.3 % for high-NO_x conditions and from 18.3 % to 42.7 % for low-NO_x conditions. SOA yields from naphthalene are in general higher compared to those from *m*-xylene, which is expected considering the larger carbon skeleton of naphthalene (Aumont et al., 2013; La et al., 2016), and are in good agreement with previous studies (Chan et al., 2009; Chen et al., 2018). However, the effect of temperature on naphthalene SOA yield is slightly lower compared to in the *m*-xylene SOA system. This may be the result of the larger carbon skeleton of naphthalene, leading to products of lower volatility that have already partitioned more in the particle phase at 295 K.

3.2 Chemical composition of oxidation products in gas and particle phases

3.2.1 *m*-Xylene

Figure 3 presents the chemical distribution of gas- (Fig. 3a and c) and particle-phase (Fig. 3b and d) products as a function of the carbon atoms following *m*-xylene oxidation by OH radicals. The mass fraction (in μg m^{-3}) is further subclassified based on the number of oxygen (Fig. 3a and b) and nitrogen atoms (Fig. 3c and d; according to the color scale),

and the molecular weight distribution was divided into three groups: m/z below 100, m/z of 101–150, and m/z above 150. The experiment was carried out under high NO_x at 280 K. The total *m*-xylene carbon balance varies from 26 % to 48 % for the gas-phase products detected depending on the oxidation conditions and considering the fact that CO, CO_2, and glyoxal are not measured. The latter compound has strong interference with the high signal of acetone. The SOA formed corresponds to 2.5 % of the total carbon balance at 295 K and 7 % at 280 K under high-NO_x conditions.

The overall product distribution at 295 K is similar to that at 280 K and can be found in Fig. S1a and b in the Supplement. At both temperatures, the gas phase is mainly composed of C_3, C_5, and C_8 products. with most having one to three O atoms, while the particle phase is dominated by C_6, C_7, and C_8 compounds generally containing two to five O atoms. In the gas phase, C_8 compounds are ring-retaining compounds related to first-generation products, while C_3 and C_5 products arise from more advanced chemistry. A larger fraction of C_3 products is present in the gas phase at 295 K when compared to 280 K (Figs. 3 and S1a). This could be due to the higher OH concentration in the experiment at 295 K (Table 1), leading to a higher consumption of C_6 and C_8 oxidation products due to their faster reactivity. This is supported by the time evolution of some compounds, such as C_6H_8O at m/z 97.06, $C_6H_6O_2$ at m/z 111.04, $C_6H_8O_4$ at m/z 145.05, and $C_8H_{10}O_5$ at m/z 187.06 (Fig. S3). This hypothesis is also backed up by previous studies reporting the reaction of oxidation products (Cappa and Wilson, 2012; Isaacman-VanWertz et al., 2018; Jin et al., 2021), while for experiments with lower OH concentration, such as at 280 K, the gas-phase products (Fig. 3a) are characterized by a higher fraction of C_8 (26 %) and C_5 (27 %) compounds.

The condensed phase is enriched in compounds with higher molecular weight when compared to the gas phase, along with the presence of four or more oxygen atoms, which highly reduces their vapor pressure (Cappa and Wilson, 2012). Particle-phase products generally exhibit an increasing trend from C_1 to C_8 (Fig. 3b), similar to the results of a recent study on toluene SOA (Lannuque et al., 2023).

The presence of NO_x may affect product distribution directly through the formation of organic nitrates or indirectly by playing a role in shaping oxidation chemistry depending on experimental conditions. The comparison of the chemical composition of gas-phase products in low NO_x and high NO_x at 295 K showed generally similar distributions (Figs. S1 and S2). The only noticeable change is the stronger contribution of C_3 and C_5 compounds in the low-NO_x experiment, resulting from the slight increase in OH radical production described above (Table 1) rather from than a real NO_x effect. This is supported by the same product distribution in the particle phase when comparing high and low NO_x, with only a small increase in organic nitrates at high NO_x. The very close distribution between high and low NO_x means that the chemistry was not strongly dependent on the NO_x regime in our experiments and that NO_x did not significantly affect the oxidant levels in the OFR.

Table 2 lists ions identified from the gas- and particle-phase products for two experiments at high NO_x at 295 and 280 K. The columns present the m/z signals measured, the assigned chemical formulas, and a tentative chemical assignment based on results from previous studies on *m*-xylene photooxidation (Atkinson et al., 1991; Forstner et al., 1997; Huang et al., 2008; Jang and Kamens, 2001; Li et al., 2018, 2022; Zhang et al., 2019a, b; Zhao et al., 2005) and on the CHARON assignment procedure recommended by Gkatzelis et al. (2018), where the average saturation mass concentration $\log_{10}(C_i^*)$ is used to discriminate between parent and fragment ions. The compounds are sorted by decreasing number of carbon atoms. For each temperature, two columns are presented: the first indicates the contribution of each compound to the total gas-phase organic products and the second the contribution to SOA. The C_8 compounds dominate both the gas and particle phases, accounting for 27 % of the total products. The most abundant C_8 gas-phase product is *m*-tolualdehyde (C_8H_8O detected at m/z 121.06), alone comprising 17 % of the reaction products. It is a first-generation ring-retaining aromatic compound previously identified in many studies (Atkinson et al., 1991; Forstner et al., 1997; Huang et al., 2008; Srivastava et al., 2023; Zhang et al., 2019b; Zhao et al., 2005). Toluic acid is a second-generation ring-retaining compound formed by the additional oxidation of *m*-tolualdehyde by the OH radical (Forstner et al., 1997; Srivastava et al., 2022, 2023), and it is a major C_8 particle-phase product ($C_8H_8O_2$ detected at m/z 137.06), contributing 5 % of the SOA mass. Another major SOA component is found at m/z 171.07 ($C_8H_{10}O_4$), tentatively assigned to dimethyl-hexadienedioic acid, a ring-opening product possibly formed by OH addition to the benzene ring followed by ring cleavage, or to dihydroxy-dimethyl-cyclohexenedione, a ring-retaining compound formed by successive OH radical reactions on the benzene ring. A second ring-opening compound is detected at m/z 155.07 ($C_8H_{10}O_3$), previously identified as dimethyl-epoxy-oxo-hexenal (Zhao et al., 2005). Other C_8 compounds are $C_8H_8O_{3-5}$ (at m/z 153.06, m/z 169.05, and m/z 185.05) and $C_8H_{10}O_5$ at m/z 187.06 (Table 2).

The contribution of C_7 compounds to the gas and particle phases accounts for 6 % and 19 %, respectively. Among the prominent C_7 products in the particle phase, we identify $C_7H_8O_2$ at m/z 125.06, tentatively assigned to dimethyl-pyranone (Forstner et al., 1997) or methyl-hexadienedial resulting from ring opening of the phenoxy radical intermediate formed via OH addition to the ring (Jang and Kamens, 2001). Further oxidation of methyl-hexadienedial will result in methyl-oxo-hexadienoic acid ($C_7H_8O_3$) at m/z 141.05 (Jang and Kamens, 2001). Another C_7 compound is $C_7H_6O_3$ at m/z 139.04, tentatively assigned to methyl cyclohexene tricarbonyls or hydroxy methyl benzoquinone, both being ring-retaining products. They can be formed by OH addi-

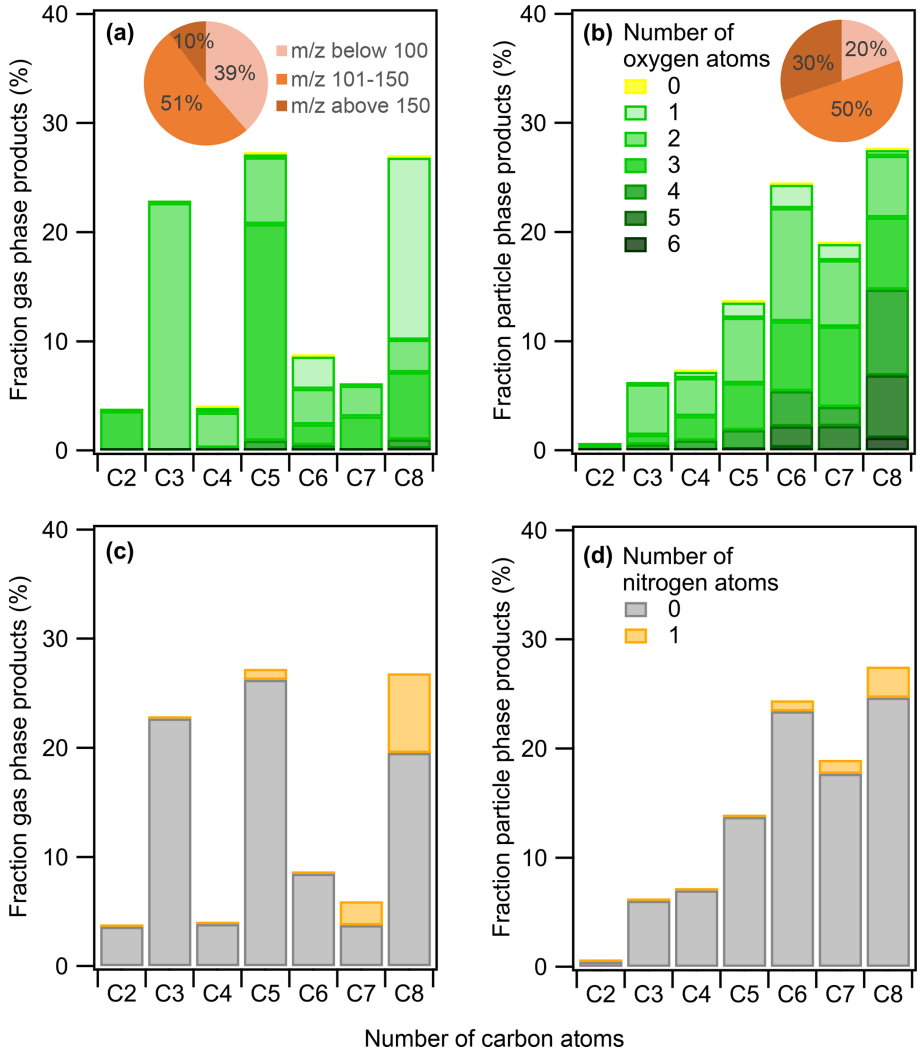

Figure 3. *m*-Xylene mass product fraction (*y* axis) distribution based on the number of carbon atoms (*x* axis) for a high-NO_x experiment at 280 K, colored by the number of **(a, b)** oxygen and **(c, d)** nitrogen atoms. The compounds detected are in the **(a, c)** gas phase and **(b, d)** particle phase. Pie charts correspond to the molecular weight contribution to the overall mass.

tion to first- or second-generation products and the release of one methyl group (Jang and Kamens, 2001). Other C_7 compounds important in the particle phase include C_7H_8O (detected at m/z 109.06), $C_7H_8O_4$ (detected at m/z 157.05), and $C_7H_8O_5$ (detected at m/z 173.04). Some of the C_7–C_8 products are nitrogen-containing compounds: nitro-*m*-xylene ($C_8H_9NO_2$ at m/z 152.07), nitrotoluene ($C_7H_7NO_2$ at m/z 138.06), dimethyl nitrophenol ($C_8H_9NO_3$ at m/z 168.06), and nitrocresol ($C_7H_7NO_3$ at m/z 154.05). The latter is the result of the NO_2 reaction with the benzyl peroxy radical in the H-abstraction route (Li et al., 2018; Srivastava et al., 2023). Aliphatic nitrogen-containing compounds are easily fragmented in the PTR-MS and thus are difficult to detect. Nevertheless, a known peroxyacetyl nitrate (PAN) fragment, $C_2H_4O_3$, detected at m/z 77.03 and also previously assigned as an unspecific fragment from the nitro-group-containing compounds has been detected (Müller et al., 2012). In total, the sum of all nitrogen-containing products (including the PAN fragment) accounted for 9 %–14 % of the gaseous-phase mass loading and 6 % of the particulate phase under high-NO_x conditions, which is close to what was seen in toluene photooxidation experiments by Lannuque et al. (2023). Under low-NO_x conditions, organic nitrates (including the PAN fragment) accounted for 4 %–12 % of the total products in the gas phase and 3 %–4 % in the particle phase, indicating limited NO_x influence on the formation of nitrogen-containing compounds (Figs. S1c, d and S2c, d). These results suggest that in our system, the shift from low to high NO_x did not substantially alter the oxidation pathways or enhance NO_x-dependent product formation.

The C_6 compounds accounted for only 6 % of the gas phase and 19 % of the organic aerosol fraction. The top

Table 2. Ions and the corresponding formulas of the major *m*-xylene products detected during photooxidation experiments under high NO_x. Reaction products are given as a fraction of the gas-phase products (in % of $\mu g\,m^{-3}$) and as a fraction of the SOA products (in % of $\mu g\,m^{-3}$). Nitrogen-containing compounds are shown in italics.

Carbon number	Measured m/z and ion sum formula	Tentative assignment	$T = 298\,K$		$T = 280\,K$	
			Gaseous products (%)	SOA products (%)	Gaseous products (%)	SOA products (%)
8	121.06 $(C_8H_8O)H^+$	*m*-tolualdehyde	13.9	0.6	16.7	0.5
8	155.07 $(C_8H_{10}O_3)H^+$	dimethyl-epoxy-oxo-hexenal/ trihydroxy dimethyl benzene	n.d.	3.8	n.d.	3.3
8	137.06 $(C_8H_8O_2)H^+$	toluic acid and possible contribution fragment at 155.07	n.d.	8.5	n.d.	5.7
8	171.07 $(C_8H_{10}O_4)H^+$	dihydroxy-dimethyl-cyclohexenedione/ dimethyl-hexadienedioic acid	0.3	4.6	0.3	5.6
8	153.06 $(C_8H_8O_3)H^+$	hydroxy dimethyl quinone	1.9	2.8	2.4	2.9
8	187.06 $(C_8H_{10}O_5)H^+$	hydroxy-cyclohexene-dicarboxylic acid oxo-cyclohexanedicarboxylic acid	0.1	2.6	0.1	2.5
8	169.05 $(C_8H_8O_4)H^+$	dihydroxy-methylbenzoic acid	n.d.	2.0	n.d.	1.6
8	185.05 $(C_8H_8O_5)H^+$	trihydroxy-(hydroxymethyl)benzaldehyde	n.d.	1.0	n.d.	0.7
8	168.06 $(C_8H_9NO_3)H^+$	*dimethyl nitrophenol*	1.9	0.4	3.6	0.4
8	152.07 $(C_8H_9NO_2)H^+$	*nitro-xylene*	0.4	0.1	1.8	0.1
7	125.06 $(C_7H_8O_2)H^+$	dimethyl-pyranone/methyl-hexadienedial	n.d.	3.6	1.6	5.0
7	141.05 $(C_7H_8O_3)H^+$	methyl-oxo-hexadienoic acid/heptenetrione	0.7	2.8	0.7	4.0
7	139.04 $(C_7H_6O_3)H^+$	hydroxy benzoic acid/hydroxy methyl benzoquinone	n.d.	3.1	n.d.	2.4
7	157.05 $(C_7H_8O_4)H^+$	hydroxy-dioxo-heptenal/epoxymethylhexenedial	n.d.	2.0	n.d.	1.8
7	109.06 $(C_7H_8O)H^+$	cresols/benzyl alcohol	n.d.	1.4	n.d.	1.5
7	173.06 $(C_7H_8O_5)H^+$	hydroxy-dioxo-heptenoic acid	n.d.	1.8	n.d.	1.2
7	138.06 $(C_7H_7NO_2)H^+$	*nitrotoluene*	1.1	0.4	1.2	0.3
7	154.05 $(C_7H_7NO_3)H^+$	*nitrocresol*	0.7	0.3	0.6	0.3
6	127.04 $(C_6H_6O_3)H^+$	hydroxymethyl furfural/hydroxyquinol/dimethylfurandione	1.0	2.4	1.4	3.3
6	113.06 $(C_6H_8O_2)H^+$	methyl-oxo-pentenal/dimethylfuranone	n.d.	1.7	0.2	2.2
6	129.06 $(C_6H_8O_3)H^+$	hydroxy-oxo-hexenal methyl-oxo-pentenoic acid	0.4	1.6	0.4	2.7
6	111.04 $(C_6H_6O_2)H^+$	methylfuraldehyde/benzenediols possible fragment at 129.06	n.d.	3.6	2.7	6.2
6	143.03 $(C_6H_6O_4)H^+$	dioxo-hexenoic acid/ methyl-dioxo-pentenoic acid tetrahydroxybenzene	n.d.	1.4	0.2	1.8
6	159.04 $(C_6H_6O_5)H^+$	oxo-hexenedioic acid	n.d.	1.2	n.d.	1.2
6	145.05 $(C_6H_8O_4)H^+$	hydroxy-dioxo hexanal	n.d.	1.2	0.1	1.1
6	115.07 $(C_6H_{10}O_2)H^+$	cyclopentylcarboxylic acid	n.d.	0.4	0.4	1.1
6	95.03 $(C_6H_6O)H^+$	phenol	n.d.	1.4	n.d.	1.2
5	113.02 $(C_5H_4O_3)H^+$	methyl-furandione	16.7	1.3	19.3	2.1
5	131.04 $(C_5H_6O_4)H^+$	methy-hydroxy-oxo-butandial	2.1	1.4	0.9	0.9
5	117.05 $(C_5H_8O_3)H^+$	oxo-pentanoic acid and fragment at 99.04	1.2	0.7	0.2	0.4
	99.04 $(C_5H_6O_2)H^+$	oxo-pentenal/methyl-butendial	6.7	3.5	2.8	3.9
5	115.03 $(C_5H_6O_3)H^+$	oxo-pentenoic acid	1.4	2.4	0.7	1.8
5	97.03 $(C_5H_4O_2)H^+$	furaldehyde	1.1	0.7	2.2	1.7

Table 2. Continued.

Carbon number	Measured m/z and ion sum formula	Tentative assignment	$T = 298$ K		$T = 280$ K	
			Gaseous Products (%)	SOA Products (%)	Gaseous Products (%)	SOA products (%)
5	101.06 $(C_5H_8O_2)H^+$ 83.05 $(C_5H_6O)H^+$	oxo-pentanal and isomers and fragment at 83.05, methylfuran	n.d 0.6	0.4 1.0	n.d 0.3	0.4 1.3
4	71.05 $(C_4H_6O)H^+$	dihydrofuran/methacrolein (MACR)/methyl vinyl ketone (MVK)	1.1	0.3	0.4	0.3
4	87.04 $(C_4H_6O_2)H^+$	butanedial/crotonic acid	n.d.	2.0	n.d.	2.2
4	103.04 $(C_4H_6O_3)H^+$	hydroxy-oxo-butanal	0.4	1.5	0.1	1.3
4	85.03 $(C_4H_4O_2)H^+$	butenedial	n.d.	1.3	n.d.	1.2
3	73.03 $(C_3H_4O_2)H^+$	methylglyoxal	20.9	3.2	9.5	2.7
3	75.04 $(C_3H_6O_2)H^+$	propanoic acid	14.3	1.7	13.3	1.6
3	89.02 $(C_3H_4O_3)H^+$	pyruvic acid/hydroxy-propanedial	1.5	0.6	n.d.	0.6
2	77.03 $(C_2H_4O_3)H^+$	PAN fragment	3.7	0.3	3.6	0.5

* n.d. = not detected.

products are ring-retaining furan-derived compounds, such as methyl-furaldehyde or benzenediols ($C_6H_6O_2$ detected at m/z 111.04) making up 3 % and 6 % of the gas and particle phases, respectively, and dimethylfurandione ($C_6H_6O_3$ detected at m/z 127.04), providing 1.4 % in the gas phase and 3.3 % in the particle phase, alongside with dimethylfuranone, providing 2.2 % in the particle phase ($C_6H_8O_2$ detected at m/z 113.06). Furanoid products can be formed through a bridged oxide intermediate on a bicyclic ring, whereas furandiones are known to originate from conjugated dicarbonyls via reaction with OH radicals followed by cyclization (Forstner et al., 1997; Jang and Kamens, 2001). Examples of unsaturated dicarbonyls and tricarbonyls in the condensed phase are methyl-oxo-pentenal ($C_6H_8O_2$ detected at m/z 113.06) and hydroxy-oxo-hexenal ($C_6H_8O_3$ detected at m/z 129.06), also assigned to methyl-oxo-pentenoic acid (Li et al., 2017, 2018; Zhao et al., 2005). Those multicarbonyls are a result of the decomposition of bicyclic alkoxy radicals (Huang et al., 2008; Zhao et al., 2005). Other C_6 compounds can be found at m/z 143.03 ($C_6H_6O_4$), 97.06 (C_6H_8O), 145.05 ($C_6H_8O_4$), and 115.07 ($C_6H_{10}O_2$) (Table 2).

As shown in Figs. 3 and S1, the C_5 products represent a major contributor to the gas phase, providing around 30 % of the total organic gaseous products and 13 % in the particle phase. In agreement with previous studies, most of the compounds are furan derivatives (Forstner et al., 1997; Jang and Kamens, 2001; Li et al., 2018). The $C_5H_4O_3$ (detected at m/z 113.02) assigned to methylfurandione alone accounts for 17 %–19 % of the gas-phase products, followed by oxopentenal and isomers ($C_5H_6O_2$ detected at m/z 99.04), with 3 %–7 % abundance. Other important products include unsaturated or oxo-aldehydes (such as $C_5H_6O_2$ at m/z 99.04 and $C_5H_6O_4$ at m/z 131.04) and organic acids such oxopentenoic acid ($C_5H_6O_3$ at m/z 115.03) (Table 2). Lannuque et al. (2023) identified dihydroxy-oxopentanoic acid (DHOPA, $C_5H_8O_5$), a known tracer of toluene and xylene SOA, in the particle phase. In our study, the DHOPA parent ion was below the detection limit, which is highly probable considering its very low formation yield (Srivastava et al., 2023) and the low precursor concentration used compared to in Lannuque et al. (2023). We therefore assume that DHOPA did not contribute significantly to the fragment ion at m/z 131.04 ($C_5H_6O_4$) that is expected upon water loss. In general, the high contribution of C_5 compounds can be explained by the *m*-xylene structure (C_8 aromatic) and the presence of two methyl groups on the benzene ring, which implies the formation of methylated furan derivatives such as methylfurandione, methyl-furanone, and furaldehyde in addition to the high contribution of C_3 compounds such as methylglyoxal, in agreement with previous studies (Birdsall and Elrod, 2011; Fan and Zhang, 2008; Forstner et al., 1997; Jang and Kamens, 2001; Li et al., 2022; Song et al., 2007; Zhang et al., 2019b).

The C_4 compounds are the least abundant in both phases (below 7 % on average) and account for shorter functionalized aldehydes, furans, and acids formed by minor pathways in the aromatic ring cleavage (Table 2). This is in agreement with the above-explained ring-opening mechanism, which mainly breaks the carbon skeleton of the xylene into C_5 and C_3 compounds instead of into two C_4 moieties (Forstner et al., 1997; Jenkin et al., 2003; Pan and Wang, 2014).

The C_3 compounds account for 23 %–37 % of the gas-phase and 6 % of the particle-phase products. Methylgly-

oxal ($C_3H_4O_2$ detected at m/z 73.03) accounts for 21 % of the gas-phase products at 295 K, while it is close to 10 % at 280 K. It makes up to 3 % of the SOA fraction and is a major second-generation product resulting from the ring cleavage of bicyclic alkoxy radicals (Fan and Zhang, 2008). Propanoic acid ($C_3H_6O_2$ detected at m/z 75.04) accounts for 8 % of the gaseous phase and only 1 % of the particle phase, as it is quite a volatile compound. This reaction product can result from the oxidation of multifunctional ring-opening products (Jang and Kamens, 2001).

3.2.2 Naphthalene

Analogously to that of *m*-xylene, Fig. 4 presents the chemical distribution of naphthalene gas-phase products (Fig. 4a and c) and particle-phase products (Fig. 4b and d) for photooxidation experiments under high-NO_x conditions at 280 K in addition to pie charts showing the molecular weight distribution. Out of the total naphthalene carbon balance, 30 %–32 % is accounted for by the gas-phase products detected under the different oxidation conditions, taking into account the fact that CO, CO_2, and glyoxal are not measured. As for the SOA formed, it corresponds to 8 % of the carbon balance under high-NO_x conditions at 295 K and 14 % at 280 K.

As the measured carbon distribution is comparable under the two temperature conditions, only the experiment at 280 K is shown in the main text (see Fig. S2 for distributions at 295 K). The gas-phase product distribution is dominated by C_{10} and C_8 compounds containing mainly two or three oxygen atoms, followed by C_3 and C_4 compounds such as methylglyoxal, resulting from the further degradation of naphthalene oxidation products. As expected, the particle phase contains more oxygen atoms and is characterized by heavy-molecular-weight compounds, with m/z above 150 comprising 75 % of the overall mass, explained by the ready partitioning of major C_{10} products containing mainly two to four oxygen atoms. Table 3 presents the major ion fragments identified, their corresponding chemical formulas, and a tentative assignment to a compound based on previous studies (Bunce et al., 1997; Chan et al., 2009; Chen et al., 2016; Kautzman et al., 2010; Lee and Lane, 2009; Nishino et al., 2009; Riva, 2013; Sasaki et al., 1997; Tomaz, 2015). Similar to what was observed in the case of *m*-xylene, the overall oxidation product distributions, including nitrogenous species (1 %–4 % in both high- and low-NO_x conditions), remain comparable across NO_x conditions (Figs. S4 and S5 at 295 K). The strong similarity in product distributions and molecular compositions implies minimal shifts in bulk volatility as well in oxidation conditions.

The C_{10} compounds account for around 15 % of the gas-phase products at both temperatures and clearly dominate the particulate phase, accounting for 59 % and 64 % of the overall aerosol mass at 295 and 280 K, respectively. The 2-formyl cinnamaldehyde ($C_{10}H_8O_2$ at m/z 161.06) is the most abundant particle-phase product, accounting for 25 % of the SOA formed at 280 K. It is assumed to be formed via two possible routes: (i) ring cleavage upon the reaction of the naphthol peroxy radical (from an OH–naphthalene adduct) with NO and (ii) a hydrogen shift from the alcohol group on the naphthol peroxy radical followed by the loss of OH and ring opening (Kautzman et al., 2010; Nishino et al., 2009; Qu et al., 2006; Sasaki et al., 1997; Wang et al., 2007). The predominance of one route over the other depends on the amount of NO_x. The 2-formyl cinnamaldehyde can further be oxidized, leading to the formation of 2-carboxy cinnamic acid ($C_{10}H_8O_4$ at m/z 193.05), the second-most-important C_{10} compound, which accounts for 8 %–15 % of the SOA mass. The oxidation of 2-formyl cinnamaldehyde also produces 2-formyl cinnamic acid ($C_{10}H_8O_3$ at m/z 177.05) (Bunce et al., 1997), which accounts for 7 %–8 % of the condensed phase. The addition of O_2 to the OH–naphthalene adduct results in the formation of epoxyquinone ($C_{10}H_6O_3$ at m/z 175.04), representing 5 %–8 % of the particle phase. Other important C_{10} ring-retaining compounds are dihydroxy naphthoquinone ($C_{10}H_6O_4$ at m/z 191.04) and 1,4-naphthoquinone ($C_{10}H_6O_2$ at m/z 159.04). This latter has multiple formation routes, from either the reaction of the OH radical with naphthalene or naphthol ($C_{10}H_8O$ at m/z 145.07) or the photodegradation of nitronaphthalene ($C_{10}H_7NO_2$ at m/z 174.05) (Atkinson et al., 1989; Kautzman et al., 2010), potentially explaining the low abundance of the latter (< 1 % in mass) alongside its reaction product with OH, nitro-naphthol ($C_{10}H_7NO_3$ at m/z 190.05). Under both high- and low-NO_x conditions, the NO_2^+ signal in the particle phase did not exceed 3 % of the aerosol mass detected by CHARON-PTR-ToF-MS, meaning that the nitro derivatives of naphthalene did not undergo strong fragmentation. In total, the sum of all nitrogen-containing products (including the PAN fragment) accounted for 2 %–3 % of the gaseous-phase mass loading and 1 %–4 % of the particulate phase under high-NO_x conditions. The low yields of nitro derivatives observed during the photooxidation of naphthalene are in agreement with previous studies (Kautzman et al., 2010; Lee and Lane, 2009; Sasaki et al., 1997). Nitronaphthol ($C_{10}H_7NO_3$ at m/z 190.05) is a well-known tracer of naphthalene SOA in high-NO_x conditions and has been observed here as a main nitrogen-containing compound. Other previously reported tracers (nitrosalicylic acid, dinitrosalicylic acid, or nitrophthalic acid) were not detected by CHARON-PTR-ToF-MS. The NO_x conditions in our study might explain why they are not formed since the formation of these compounds is NO_x dependent and our study used lower NO_x levels compared to studies using HONO or CH_3NO as the OH radical precursors, for example (Sato et al., 2022). We should also consider that the UV lights used, which peaked at 310 nm, may induce photolysis of nitronaphthalene and other nitro derivatives, as has been previously reported in chamber experiments with similar UV lamps (Healy et al., 2012).

Table 3. List of ions and the corresponding formulas of the major naphthalene products detected during photooxidation experiments under high NO_x. Reaction products are given as a fraction of the gas-phase products (in % of $\mu g\,m^{-3}$) and as a fraction of the SOA products (in % of $\mu g\,m^{-3}$). Nitrogen-containing compounds are shown in italics.

Carbon number	Measured m/z and ion sum formula	Tentative assignment	$T = 295\,K$		$T = 280\,K$	
			Gaseous products (%)	SOA products (%)	Gaseous products (%)	SOA products (%)
10	161.06 $(C_{10}H_8O_2)H^+$	formyl cinnamaldehyde	2.0	8.9	3.5	25.4
10	193.05 $(C_{10}H_8O_4)H^+$	carboxy cinnamic acid	0.8	15.3	1.0	8.1
10	159.04 $(C_{10}H_6O_2)H^+$	naphthoquinone	6.6	5.6	4.9	9.3
10	177.05 $(C_{10}H_8O_3)H^+$	formyl cinnamic acid	0.6	7.7	1.1	7.1
10	175.04 $(C_{10}H_6O_3)H^+$	epoxy-naphthoquinone	1.6	8.4	1.9	4.8
10	145.07 $(C_{10}H_8O)H^+$	naphthol	0.4	2.2	0.5	3.6
10	191.04 $(C_{10}H_6O_4)H^+$	dihydroxy naphthoquinone	0.7	3.5	0.8	2.0
10	195.06 $(C_{10}H_{10}O_4)H^+$	carboxybenzenepropanoic acid benzofurancarboxyaldehyde	0.3	1.5	0.3	1.0
10	174.05 $(C_{10}H_7NO_2)H^+$	*nitronaphthalene*	1.2	0.3	0.3	0.2
10	190.05 $(C_{10}H_7NO_3)H^+$	*nitronaphthol*	0.5	2.5	0.1	0.4
9	147.05 $(C_9H_6O_2)H^+$	benzopyrone	3.5	8.3	1.9	5.8
9	163.04 $(C_9H_6O_3)H^+$	hydroxycoumarin	1.5	6.3	2.2	4.5
9	133.06 $(C_9H_8O)H^+$	indanone	1.6	1.3	1.3	3.6
9	179.04 $(C_9H_6O_4)H^+$	dihydroxy-indanedione	0.5	4.2	0.1	2.8
9	165.06 $(C_9H_8O_3)H^+$	hydroxy cinnamic acid	0.9	2.7	0.6	1.8
9	181.05 $(C_9H_8O_4)H^+$	dihydroxy cinnamic acid	0.2	1.5	0.2	0.9
8	135.05 $(C_8H_6O_2)H^+$	phthaldialdehyde/phthalide	19.3	3.9	5.4	4.3
8	149.03 $(C_8H_4O_3)H^+$	phthalic anhydride	13.8	3.3	9.9	2.0
8	151.04 $(C_8H_6O_3)H^+$	hydroxy phthaldehyde hydroxy phthalide	0.5	1.2	1.0	3.7
7	123.05 $(C_7H_6O)H^+$	benzoic acid	1.9	0.2	1.4	0.1
7	107.05 $(C_7H_6O)H^+$	benzaldehyde	1.0	n.d.	0.9	n.d.
6	111.05 $(C_6H_6O_2)H^+$	catechol/benzoquinone	1.2	n.d.	0.9	n.d.
6	115.07 $(C_6H_{10}O_2)H^+$	dimethyloxolan-one/ hexanedione	1.3	0.3	1.3	0.6
5	101.06 $(C_5H_8O_2)H^+$	methyl furan	0.7	n.d.	1.6	n.d.
4	89.06 $(C_4H_8O_2)H^+$	hydroxybutanone/hydroxybutanal	10.1	0.1	11.5	n.d.
4	71.05 $(C_4H_6O)H^+$	dihydrofuran/MACR/MVK	1.2	n.d.	1.8	n.d.
3	75.04 $(C_3H_6O_2)H^+$	propanoic acid	12.3	0.3	19.9	0.2
3	73.03 $(C_3H_4O_2)H^+$	methylglyoxal	3.6	0.1	5.4	0.1
2	77.02 $(C_2H_4O_3)H^+$	PAN fragment	2.0	0.1	1.3	0.1

* n.d. = not detected

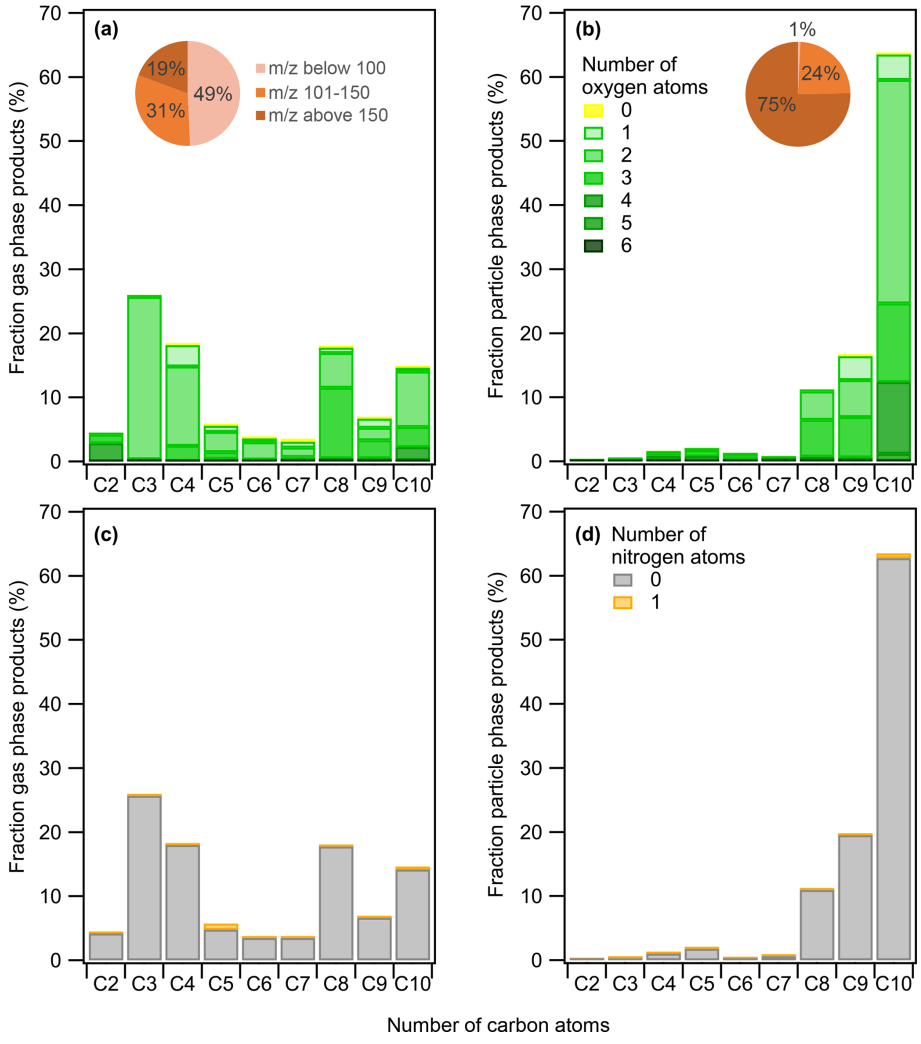

Figure 4. Naphthalene mass product fraction (y axis) distribution based on the number of carbon atoms (x axis) for a high-NO_x experiment at 280 K, colored by the number of **(a, b)** oxygen and **(c, d)** nitrogen atoms. The compounds detected are in the **(a, c)** gas phase and **(b, d)** particle phase. Pie charts correspond to the molecular weight contribution to the overall mass.

The formation of C_9 and C_7 products can be explained by H abstraction of 2-formyl cinnamaldehyde, leading to a formyl peroxy radical that subsequently reacts with NO to form an alkoxy radical, implying the loss of the CO_2 group (Kautzman et al., 2010). The C_9 compounds contribute 6 %–9 % to the gas phase and are the second-highest contributors to the particle phase, providing 16 %–20 % of the total organic mass. The chemical formulas identified include $C_9H_6O_2$ (at m/z 147.05), which can be either benzopyrone (also known as coumarin) or indene-dione, as well as indanone (C_9H_8O at m/z 133.06), which was first detected by Lee and Lane (2009). No formation mechanism has been proposed for these products so far, but their molecular structure clearly indicates a rearrangement following ring opening, forming a new ring at either six atoms including one oxygen in the case of coumarin or five atoms for the indene-dione and indanone. This ring closure is a common feature in the case of oxidation of dialdehydes, as explained by Lannuque and Sartelet (2024), which may support the hypothesis that these compounds originated from 2-formyl cinnamaldehyde. Further photooxidation of coumarin may lead to hydroxycoumarin ($C_9H_6O_3$ at m/z 163.04), accounting for 2.2 % of the gas phase and 4 %–6 % of the particle phase. A more oxygenated compound, dihydroxy-indanedione ($C_9H_6O_4$ at m/z 179.04), was previously identified by Lee and Lane (2009). Logically, this compound was mainly present in the condensed phase, providing 3 %–4 % of the total SOA mass.

C_8 oxidation products make up a good 18 %–35 % and 10 %–11 % of the gas and particle phases, respectively. Phthaldialdehyde and phthalic anhydride largely dominate the C_8 compounds and are of particular importance in the gas phase. Phthaldialdehyde ($C_8H_6O_2$ at m/z 135.05) is both a first- and second-generation ring-opening product of the OH radical reaction with naphthalene, with the second-

generation pathway expected to originate from the reaction of the OH radical with 2-formyl cinnamaldehyde (Sasaki et al., 1997; Wang et al., 2007). Further addition of the OH radical to phthaldialdehyde will lead to hydroxy phthaldehyde/hydroxy phthalide ($C_8H_6O_3$ at m/z 151.04), which makes up 3.7 % of SOA (Table 3), while H abstraction followed by intramolecular cyclization results in phthalic anhydride ($C_8H_4O_3$ at m/z 149.03), making up 2 %–3 % of the condensed phase and 10 %–14 % in gas phase (Table 3), which was previously observed by Wang et al. (2007).

C_7 compounds are relatively less abundant, accounting for 3 % of the gas-phase products and less than 1 % of SOA. They include compounds like benzoic acid ($C_7H_6O_2$ at m/z 123.05) and benzaldehyde (C_7H_6O at m/z 107.05).

Only two C_6 compounds are detected and represent 3 %–4 % of the total gas products and only 1 % of the SOA yield. The dominant C_6 compound in the gaseous phase is $C_6H_{10}O_2$ (at m/z 115.07), providing 1.3 %, which can be dimethyloxolanone or hexanedione. The former can be formed from the oxidation of phthaldialdehyde, implying the opening of the second aromatic cycle (Kautzman et al., 2010). Another minor C_6 compound is catechol or benzoquinone ($C_6H_{10}O_2$ at m/z 115.07).

C_5 products account for only 3 %–6 % of the gaseous phase and less than 2 % of SOA. A major compound detected is $C_5H_8O_2$ at m/z 101.06 (1.6 %), which can be assigned to methyl furan or 4-oxopentanal. The C_2–C_4 products are more volatile, all together making less than 2 % of the total SOA mass, but present a considerable fraction of the gas-phase products, providing 18 % for C_4, 26 % for C_3, and 4 % for C_2. The major C_4 contributor is $C_4H_8O_2$ (at m/z 89.06), representing 12 % of the gas-phase products. It is tentatively assigned to hydroxybutanal or butanoic acid. Almost all of the C_3 fraction is represented by propanoic acid ($C_3H_6O_2$ at m/z 75.04), with a 12 %–20 % contribution to the gas-phase products, and methylglyoxal ($C_3H_4O_2$ at m/z 73.03), representing up to 5 %. The C_2 compound is tentatively assigned to the PAN fragment $C_2H_4O_3$ detected at m/z 77.02 (1.4 %) (Müller et al., 2012).

3.3 Experimentally derived and estimated gas–particle phase partitioning

A two-dimensional space, the 2D-VBS framework (Donahue et al., 2011; Murphy et al., 2012), is used as a means to visualize the compound distributions as a function of the experimentally derived volatility ($\log_{10}C_i^*$) and the O/C ratio (Fig. 5) or the oxidation state of carbon (OSc) (Fig. S4). Such a molecular-level effect of temperature on SOA for *m*-xylene and naphthalene is reported here for the first time. Figure 5a and b display the distribution of the volatilities measured for the major compounds detected in both the gas and particle phases for *m*-xylene and naphthalene under high-NO_x conditions. The volatilities of the compounds identified are in the range of SVOCs with C_i^* values ranging from 0.3 to 300 µg m^{-3} (vapor pressures approximately $10^{-8} - 10^{-5}$ Torr) to IVOCs with C_i^* values ranging from 300 to 3×10^6 µg m^{-3} (vapor pressures approximately 10^{-5}–10^{-1} Torr) (Donahue et al., 2012), indicated by the light-green ($\log_{10}C_i^*$ from 0 to 2.5) and light-blue ($\log_{10}C_i^*$ from 2.5 to 5) background shading, respectively. Data points are indicated for the experiments at 280 K (purple circles) and 295 K (red circles), and the size of the circles is proportional to the mass concentration (in µg m^{-3}) of each ion in the particle phase.

For *m*-xylene, out of the approximately 110 ions detected in the particle phase, half of them are found exclusively in the particle phase. This fraction should populate a low-volatility area (as ELVOCs), and it is not represented in the 2D-VBS (Fig. 5a) but represents more than 30 % of the SOA mass. Among the remaining ions that partition between the two phases, only 18 are considered in Fig. 5a because they are either important in terms of mass or are considered parent ions, following the Gkatzelis et al. (2018) method. About 24 %–58 % of the particle mass populates the SVOC regime, while 8 %–16 % is in the IVOC regime, depending on the experimental conditions. In recent work, the SOA components from OH radical oxidation of toluene populated mostly the SVOC range, and only 10 %–17 % was exclusively in the particle phase (Lannuque et al., 2023), probably because of higher initial VOC concentrations and lower OH exposure (10–20 h compared to 1.3–3 d in this study), leading to less advanced oxidation. But overall, the effect of temperature that we observed is quite similar for the two chemical systems. For naphthalene at 280 K, out of the 110 ions detected in the particle phase, 40 ions are exclusively observed in the particle phase, making up only 5 % of the condensed mass fraction. For the 20 compounds selected that partition between the two phases, approximately 78 %–95 % of their SOA mass populates the SVOC regime, and 3 %–17 % lies in the IVOC portion. The larger skeleton structure of naphthalene oxidation products, even in the first generation, can explain the high fraction of SOA in the SVOC regime (predominantly C_{8-10} compounds), as confirmed by the O/C range being lower for naphthalene than for *m*-xylene.

The saturation concentration (C_i^*) values that we derived range between 1 and 6919 µg m^{-3}, comparable to other SOA systems (Gkatzelis et al., 2018; Kostenidou et al., 2024; Lannuque et al., 2023). Previous studies on biogenic VOCs reported decreasing volatility with increasing OSc (Gkatzelis et al., 2018; Jimenez et al., 2009; Kroll et al., 2011), while the present work and previous investigations of anthropogenic VOCs (toluene and gasoline vehicle emissions) did not confirm such a trend (Kostenidou et al., 2024; Lannuque et al., 2023).

Figure 5c and d present the differences in $\log_{10}C_i^*$ between the two experiments conducted at 280 and 295 K: $\Delta\log_{10}C_i^*$. Its values vary from 0.06 to 1.08 as a function of carbon number and oxygen number (Tables S2 and S3). For *m*-xylene

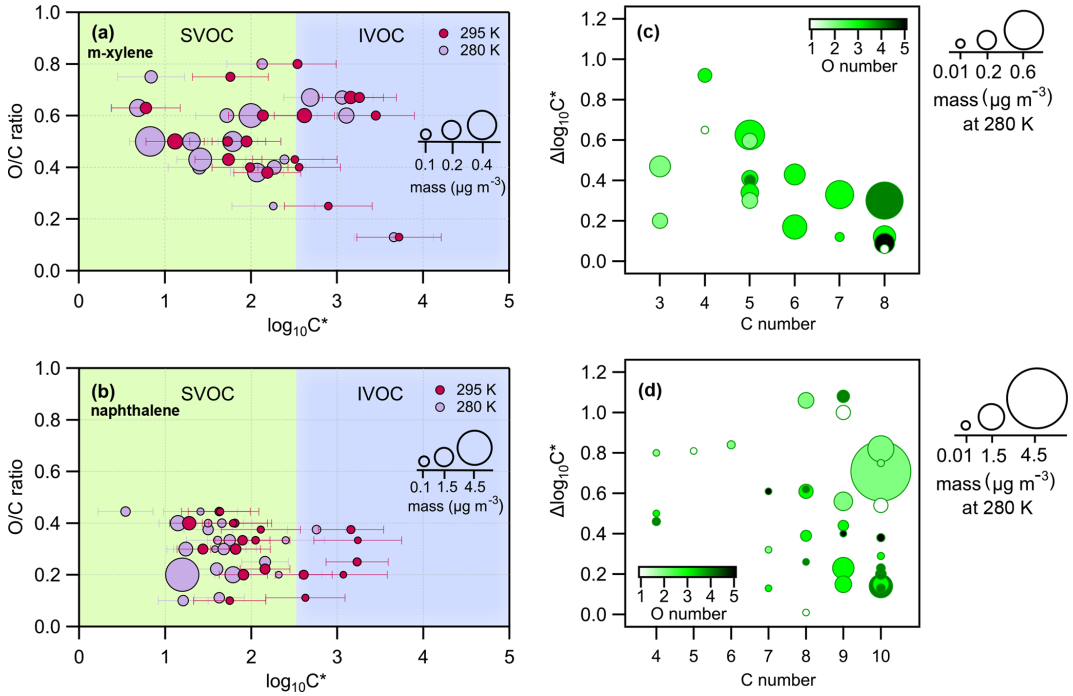

Figure 5. Panels **(a)** and **(b)** present the 2D-VBS framework: the O/C ratio (y axis) for the parent ions of m-xylene and naphthalene photooxidation, respectively, as a function of the saturation concentration ($\log_{10}C_i^*$ in µg m^{-3}, x axis) for the high-NO$_x$ experiments. The size of the circles denotes the mass of each species. Experiments carried out at 280 K are in light violet, while the ones carried out at 295 K are in magenta. The light-green and light-blue background shading corresponds to the SVOC ($0 < \log_{10}C_i^* < 2.5$) and the IVOC ($2.5 < \log_{10}C_i^* < 5$) regimes, respectively. Panels **(c)** and **(d)** present $\Delta\log_{10}C_i^*$ for m-xylene and naphthalene oxidation products, respectively (the difference in $\log_{10}C_i^*$ between experiments at 280 and 295 K, y axis), as a function of the carbon number (x axis), color scaled by the oxygen number and sized by the mass (in µg m^{-3}) of each compound at 280 K.

oxidation products (Fig. 5c), $\Delta\log_{10}C_i^*$ decreases with increasing carbon number. Indeed, the C_5–C_8 products bearing three to five oxygen atoms (darker-green markers) lie at the bottom of the plot, generally exhibiting $\Delta\log_{10}C_i^*$ values below 0.4, emphasizing the effect of oxygen atoms on the reduction of the volatility of these compounds. The C_3 compounds tentatively associated with methylglyoxal and propanoic acid also exhibit moderate $\Delta\log_{10}C_i^*$, probably because they are still volatile even at the lower experimental temperatures (Table 2). Only a few among the C_4–C_5 products identified exhibit $\Delta\log_{10}C_i^*$ values above 0.6 and are tentatively identified as ring-opening products, with multiple functional groups increasing their polarity (aldehydes, acids, and furandiones).

Naphthalene oxidation products, on the other hand (Fig. 5d), have $\Delta\log_{10}C_i^*$ over a similar range compared to m-xylene but exhibit different behavior. Most of the relevant reaction products are associated with $C_{8-10}H_{4-10}O_{1-4}$ products, accounting for 90 % of the SOA mass and having at least one aromatic ring. These compounds belong to SVOCs with a $\log_{10}C_i^* < 2$ and span a broad range of $\Delta\log_{10}C_i^*$ depending on the number of oxygen atoms (from one to five) and the specific functionalities. Logically, the most oxygenated C_{10} compounds are not very affected by temperature since they are the least volatile and are already mostly in the particle phase at 295 K. Compared to m-xylene, the most important naphthalene SOA products are less oxygenated and seem to be more temperature sensitive.

3.4 Comparison of experimentally derived and calculated volatilities

The experimentally derived volatilities are here compared to the estimated ones from pure-liquid saturation vapor pressure using Volcalc based on SIMPOL.1 (Meredith et al., 2023; Pankow and Asher, 2008; Riemer, 2023). Volatilities from the two methods are presented in Fig. 6a and b for both m-xylene and naphthalene oxidation products at 280 K, respectively. A considerable discrepancy is observed between the experimental and calculated values, with the latter ones spanning a larger range of volatilities. For m-xylene SOA, the theoretical approach tends to largely overestimate the volatility of small and oxygenated compounds below m/z 120 in a similar way to recent investigations using different techniques, such as SV-TAG coupled to GC-MS, thermal desorption AMS, and FIGAERO-CIMS and CHARON (Stark et al., 2017; Ijaz et al., 2024; Liang et al., 2023).

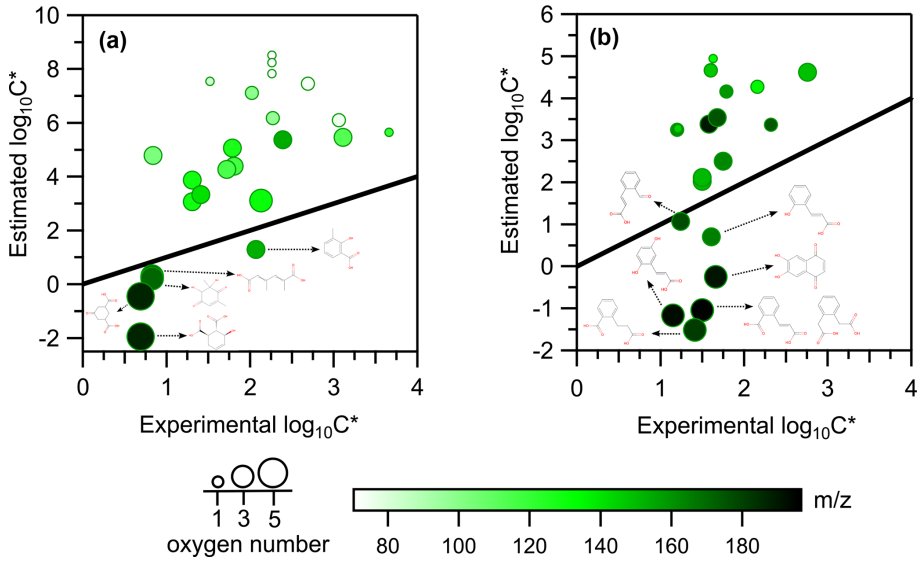

Figure 6. Theoretical (y axis) vs. experimental (x axis) $\log_{10}C_i^*$ values for **(a)** m-xylene and **(b)** naphthalene oxidation products at 280 K under high-NO_x conditions. The black line is the 1 : 1 fit. The size of the markers is proportional to the oxygen number. The color gradient corresponds to the m/z of the compounds detected.

For some light carbonyl compounds present among the m-xylene reaction products, the disagreement can potentially be explained by the presence of ammonium ions (NH_4^+) in the seeds, which can act as a catalyst for accretion reactions such as aldol condensation (Li et al., 2022, 2011; Nozière et al., 2010; Sareen et al., 2010) as well as acetal and hemiacetal formation (Jang et al., 2002; Li et al., 2022; Loeffler et al., 2006; Shapiro et al., 2009), shifting the equilibrium to the condensed phase for these molecules. Furthermore, Lannuque et al. (2023) achieved better model representation of experimental SOA mass concentration after including interactions between aldehydes (such as methylglyoxal) and inorganic compounds (such as ammonium). Those reactions are also catalyzed in the presence of water, especially for highly oxidized hydrophilic compounds (Meng et al., 2024). For some other compounds, such as functionalized acids and some dialdehydes, disagreements may arise from the fragmentation in the mass spectrometer. Despite the relatively low E/N value (68 Td) used in this work, fragmentation may still occur, particularly in polyfunctional products (Leglise et al., 2019). We also tested the fragmentation of several compounds in a separate work (Lannuque et al., 2023), where we were able to observe low or negligible fragmentation of methylglyoxal, furans, furfurals, maleic acids, and anhydrides but observed important fragmentation of small linear aldehydes.

For naphthalene SOA products, larger discrepancies are observed for the larger compounds ($m/z \geq 160$) associated with C_{8-10} compounds bearing multiple functional groups. For such types of compounds, the model predicts very low volatility (O'Meara et al., 2014), also demonstrating the fact that SIMPOL.1 consistently overestimates temperature-induced volatility changes for highly oxygenated compounds (such as hydroxylated ketones and diacids). These discrepancies are attributed to the additive nature of SIMPOL.1's functional group contribution framework. At 280 K, a carboxylic acid group (–COOH) decreases the saturation vapor pressure by nearly a factor of 6000, a hydroxyl group (–OH) by a factor of 200, and a ketone group (=O) by less than a factor of 9. It is also worth noting that multiple structural isomers are not distinguished in our work, and this may also introduce some uncertainties. An example is provided by the 1,2-naphthoquinone and 1,4-naphthoquinone caused by quite different vapor pressures, making the former potentially more interesting in the particle phase (McWhinney et al., 2013). Liang et al. (2023) and Dang et al. (2019) also reported very different gas–particle partitioning behavior and vapor pressures values among isomers. Barley and McFiggans (2010) and Peräkylä et al. (2020) highlighted significant overpredictions for diacids and polyfunctional compounds, attributing these errors to the model's parameterizations and group contributions. This work therefore aligns with previous findings and suggests that vapor pressures of multifunctional compounds of the aerosol are still not estimated well by models.

Figure S7 shows the comparison of estimated vs. experimental $\log_{10}C_i^*$ values at 295 K under high-NO_x conditions for both m-xylene and naphthalene. These results closely match those at 280 K (Fig. 6), with no significant difference in the distribution. Figure S8 presents the same analysis under low-NO_x conditions at 295 K, which similarly shows no notable deviation from the trends observed at low NO_x (Fig. S7). This indicates that neither temperature nor the NO_x regime substantially explains the model–observation discrep-

ancy in our dataset. Temperature-induced volatility changes are quantified in Fig. 5c and d, which represent the differences between the experimental $\log_{10}C_i^*$ at 280 and 295 K (i.e., $\Delta\log_{10}C_i^*$) compared to the C number. The temperature effect on the discrepancies between the experimental and the estimated $\log_{10}C_i^*$ values is presented in Fig. S9. The values of $\Delta\log_{10}C_i^*$, the difference between the estimated and experimental $\log_{10}C_i^*$, for the oxidation products of *m*-xylene (Fig. S9a) and naphthalene (Fig. S9b), is plotted as a function of m/z at 295 and 280 K. The discrepancies at both temperatures are quite close to each other. Overall, SIMPOL.1's bias in predicting volatility for oxidation products is not strongly affected by temperature. This consistent discrepancy related to temperature and NO_x confirmed that the partitioning of organic compounds is more complex than the simple evaporation of the compounds isolated and that surface interactions and bulk chemical reactions are potentially important drivers affecting partitioning equilibria.

4 Conclusion

This study presents a detailed experimental investigation of the OH-initiated photooxidation of two anthropogenic aromatic precursors, *m*-xylene and naphthalene, using an OFR under different NO_x and temperature conditions. For both precursors, SOA yields are found to strongly increase when temperature and NO_x decrease, in agreement with previous studies. The CHARON inlet coupled to a PTR-ToF-MS successfully quantified between 65 % and 80 % of the total organic mass covered by an aerosol mass spectrometer (HR-ToF-AMS). Major products in both the gas and particulate phases are confirmed based on the PTR-ToF-MS-inferred molecular formula and on an intercomparison with the literature. Major gas-phase products of *m*-xylene SOA are C_3, C_5, and C_8 compounds, whereas the particle-phase products are dominated by C_6–C_8 compounds. This pattern is consistent under different temperatures, indicating similar chemistry under these conditions. For naphthalene experiments, gas-phase products are dominated by C_8 and C_{10} compounds, while the particle-phase composition mainly consists of C_8, C_9, and C_{10} compounds. Nitro derivatives (nitrogen-containing compounds and the PAN fragment) measured in both phases did not exceed 7 % in naphthalene experiments, whereas they reached up to 20 % in the *m*-xylene experiments. The similarity in product distributions under both high- and low-NO_x conditions for both *m*-xylene and naphthalene indicates that the chemical reactions were largely unaffected by the NO_x levels, implying that NO_x had a minimal influence on oxidant concentrations in the OFR.

The volatility properties of the individual compounds are presented in the 2D-VBS framework: 24 %–58 % of the SOA mass generated by *m*-xylene populates the SVOC regime and 8 %–16 % populates the IVOC regime, while the naphthalene SOA mass is mostly (up to 95 %) found in the SVOC regime. No clear correlation was observed between the volatility values and the increasing oxidation state (OSc), in agreement with previous studies on anthropogenic monoaromatic precursors. Temperature variation from 295 to 280 K induced an expected decrease in volatility ($\Delta\log_{10}C_i^*$), this decrease ranging from 0.06 to 1.08. The magnitude of $\Delta\log_{10}C_i^*$ seems to be controlled by multiple parameters, such as temperature, carbon number, oxygen number, and specific chemical moieties. When experimentally derived volatilities are compared to a group contribution parameterization model based on pure-liquid vapor pressure (SIMPOL.1), large discrepancies are observed. The small discrepancies between estimated and experimental $\log_{10}C_i^*$ at both temperatures indicate that the temperature has little impact on SIMPOL.1's bias when predicting the volatility of oxidation products. The difference between estimated and experimental volatilities highlights the complexity of gas–particle partitioning and the limits of parameterizations that should be further validated using larger datasets from various measurement techniques and experimental conditions.

This study advances our understanding of SOA composition and gas–particle partitioning under different and relevant atmospheric conditions and also holds some implications for urban air quality management and climate modeling. The observed temperature-dependent shifts in SOA mass loadings and volatility highlight the importance of accounting for seasonal variations, particularly in urban areas with high anthropogenic VOC emissions. Furthermore, the findings underscore the need to refine current air quality and climate models by incorporating more recent findings and real-world atmospheric conditions, paving the way for more accurate predictions of aerosol impacts on air quality, climate, and public health.

Data availability. Finalized data are mostly available in the Supplement. More detailed data are available on request.

Supplement. The supplement related to this article is available online at https://doi.org/10.5194/acp-25-10267-2025-supplement.

Author contributions. MS, JK, and BD designed the experimental setup. MS, JK, BTR, and BD performed the experiments and data treatment. MS, BD, and JK analyzed and interpreted the data. MS ran the SIMPOL.1 model. MS drafted the article. All co-authors revised the article.

Competing interests. The contact author has declared that none of the authors has any competing interests.

Financial support. This work was funded by the POLEMICS project of the Agence Nationale de la Recherche (ANR) program (grant no. ANR-18-CE22-0011); the MAESTRO-EU6 project (ADEME CORTEA grant no. 1866C0001); the French government under the France 2030 investment plan, as part of the Initiative d'Excellence d'Aix-Marseille Université – A*MIDEX (grant no. AMX-21-PEP-016); the French national research agency (grant no. ANR-22-CE22-0003-01); and the Environmental Sciences doctoral school (grant no. ED 251). Barbara D'Anna was supported by the MITI program from CNRS, allowing the design and construction of the new oxidation flow reactor (OFR) deployed in this study.

Review statement. This paper was edited by Ivan Kourtchev and reviewed by four anonymous referees.

References

Ahn, J., Rao, G., and Vejerano, E.: Temperature dependence of the gas-particle partitioning of selected VOCs, Environ. Sci.-Proc. Imp., 23, 947–955, https://doi.org/10.1039/D1EM00176K, 2021.

Anderson, J. O., Thundiyil, J. G., and Stolbach, A.: Clearing the Air: A Review of the Effects of Particulate Matter Air Pollution on Human Health, J. Med. Toxicol., 8, 166–175, https://doi.org/10.1007/s13181-011-0203-1, 2012.

Atkinson, R., Aschmann, S. M., and Zielinska, B.: Gas-phase atmospheric chemistry of l- and 2-nitronaphthalene and 1,4-naphthoquinone, Atmos. Environ., 23, 2679–2690, https://doi.org/10.1016/0004-6981(89)90548-9, 1989.

Atkinson, R., Aschmann, S. M., and Arey, J.: Formation of ring-retaining products from the OH radical-initated reactions of *o*-, *m*-, and *p*-xylene, Int. J. Chem. Kinet., 23, 77–97, https://doi.org/10.1002/kin.550230108, 1991.

Aumont, B., Camredon, M., Mouchel-Vallon, C., La, S., Ouzebidour, F., Valorso, R., Lee-Taylor, J., and Madronich, S.: Modeling the influence of alkane molecular structure on secondary organic aerosol formation, Faraday Discuss., 165, 105, https://doi.org/10.1039/c3fd00029j, 2013.

Bahrami, A., Haghighat, F., and Zhu, J.: Indoor environment gas-particle partitioning models of SVOCs and impact of particle properties on the partitioning: A review, Build Environ., 262, N.PAG, https://doi.org/10.1016/j.buildenv.2024.111791, 2024.

Barley, M. H. and McFiggans, G.: The critical assessment of vapour pressure estimation methods for use in modelling the formation of atmospheric organic aerosol, Atmos. Chem. Phys., 10, 749–767, https://doi.org/10.5194/acp-10-749-2010, 2010.

Berlinger, B., Fehérvári, P., Kővágó, C., Lányi, K., Mátis, G., Mackei, M., and Könyves, L.: There Is Still a Need for a Comprehensive Investigation of the Health Consequences of Exposure to Urban Air with Special Regard to Particulate Matter (PM) and Cardiovascular Effects, Atmosphere, 15, 296, https://doi.org/10.3390/atmos15030296, 2024.

Birdsall, A. W. and Elrod, M. J.: Comprehensive NO-Dependent Study of the Products of the Oxidation of Atmospherically Relevant Aromatic Compounds, J. Phys. Chem. A, 115, 5397–5407, https://doi.org/10.1021/jp2010327, 2011.

Bloss, C., Wagner, V., Jenkin, M. E., Volkamer, R., Bloss, W. J., Lee, J. D., Heard, D. E., Wirtz, K., Martin-Reviejo, M., Rea, G., Wenger, J. C., and Pilling, M. J.: Development of a detailed chemical mechanism (MCMv3.1) for the atmospheric oxidation of aromatic hydrocarbons, Atmos. Chem. Phys., 5, 641–664, https://doi.org/10.5194/acp-5-641-2005, 2005.

Bosque, R. and Sales, J.: Polarizabilities of Solvents from the Chemical Composition, J. Chem. Inf. Comp. Sci., 42, 1154–1163, https://doi.org/10.1021/ci025528x, 2002.

Bunce, N. J., Liu, L., Zhu, J., and Lane, D. A.: Reaction of Naphthalene and Its Derivatives with Hydroxyl Radicals in the Gas Phase, Environ. Sci. Technol., 31, 2252–2259, https://doi.org/10.1021/es960813g, 1997.

Calvert, J. G., Atkinson, R., Becker, K. H., Kamens, R. M., Wallington, T. H., Seinfeld, J. H., and Yarwood, G.: The Mechanisms of Atmospheric Oxidation of Aromatic Hydrocarbons, Oxford University Press, ISBN 978-0-19-514628-8, 2002.

Calvert, J. G., Orlando, J. J., Stockwell, W. R., and Wallington, T. J.: The Mechanisms of Reactions Influencing Atmospheric Ozone, Oxford University Press, https://doi.org/10.1093/oso/9780190233020.001.0001, 2015.

Canagaratna, M. R., Jayne, J. T., Jimenez, J. L., Allan, J. D., Alfarra, M. R., Zhang, Q., Onasch, T. B., Drewnick, F., Coe, H., Middlebrook, A., Delia, A., Williams, L. R., Trimborn, A. M., Northway, M. J., DeCarlo, P. F., Kolb, C. E., Davidovits, P., and Worsnop, D. R.: Chemical and microphysical characterization of ambient aerosols with the aerodyne aerosol mass spectrometer, Mass Spectrom. Rev., 26, 185–222, https://doi.org/10.1002/mas.20115, 2007.

Cappa, C. D. and Wilson, K. R.: Multi-generation gas-phase oxidation, equilibrium partitioning, and the formation and evolution of secondary organic aerosol, Atmos. Chem. Phys., 12, 9505–9528, https://doi.org/10.5194/acp-12-9505-2012, 2012.

Chan, A. W. H., Kautzman, K. E., Chhabra, P. S., Surratt, J. D., Chan, M. N., Crounse, J. D., Kürten, A., Wennberg, P. O., Flagan, R. C., and Seinfeld, J. H.: Secondary organic aerosol formation from photooxidation of naphthalene and alkylnaphthalenes: implications for oxidation of intermediate volatility organic compounds (IVOCs), Atmos. Chem. Phys., 9, 3049–3060, https://doi.org/10.5194/acp-9-3049-2009, 2009.

Chen, C.-L., Kacarab, M., Tang, P., and Cocker, D. R.: SOA formation from naphthalene, 1-methylnaphthalene, and 2-methylnaphthalene photooxidation, Atmos. Environ., 131, 424–433, https://doi.org/10.1016/j.atmosenv.2016.02.007, 2016.

Chen, C.-L., Li, L., Tang, P., and Cocker, D. R.: SOA formation from photooxidation of naphthalene and methylnaphthalenes with *m*-xylene and surrogate mixtures, Atmos. Environ., 180, 256–264, https://doi.org/10.1016/j.atmosenv.2018.02.051, 2018.

Chen, T., Liu, Y., Chu, B., Liu, C., Liu, J., Ge, Y., Ma, Q., Ma, J., and He, H.: Differences of the oxidation process and secondary organic aerosol formation at low and high precursor concentrations, J. Environ. Sci., 79, 256–263, https://doi.org/10.1016/j.jes.2018.11.011, 2019.

Chen, T., Chu, B., Ma, Q., Zhang, P., Liu, J., and He, H.: Effect of relative humidity on SOA formation from aromatic hydrocarbons: Implications from the evolution of gas- and particle-phase species, Sci. Total Environ., 773, 145015, https://doi.org/10.1016/j.scitotenv.2021.145015, 2021.

Clark, C. H., Kacarab, M., Nakao, S., Asa-Awuku, A., Sato, K., and Cocker, D. R.: Temperature Effects on Secondary Organic Aerosol (SOA) from the Dark Ozonolysis and Photo-Oxidation of Isoprene, Environ. Sci. Technol., 50, 5564–5571, https://doi.org/10.1021/acs.est.5b05524, 2016.

Dang, C., Bannan, T., Shelley, P., Priestley, M., Worrall, S. D., Waters, J., Coe, H., Percival, C. J., and Topping, D.: The effect of structure and isomerism on the vapor pressures of organic molecules and its potential atmospheric relevance, Aerosol Sci. Tech., 53, 1040–1055, https://doi.org/10.1080/02786826.2019.1628177, 2019.

DeCarlo, P. F., Kimmel, J. R., Trimborn, A., Northway, M. J., Jayne, J. T., Aiken, A. C., Gonin, M., Fuhrer, K., Horvath, T., Docherty, K. S., Worsnop, D. R., and Jimenez, J. L.: Field-Deployable, High-Resolution, Time-of-Flight Aerosol Mass Spectrometer, Anal. Chem., 78, 8281–8289, https://doi.org/10.1021/ac061249n, 2006.

Deng, Y., Inomata, S., Sato, K., Ramasamy, S., Morino, Y., Enami, S., and Tanimoto, H.: Temperature and acidity dependence of secondary organic aerosol formation from α-pinene ozonolysis with a compact chamber system, Atmos. Chem. Phys., 21, 5983–6003, https://doi.org/10.5194/acp-21-5983-2021, 2021.

Dodge, M.: Combined use of modeling techniques and smog chamber data to derive ozone-precursor relationships, International conference on photochemical oxidant pollution and its control: Proceedings, Research Triangle Park, NC, 12–17 September 1976, 881–889, 1977.

Donahue, N. M., Robinson, A. L., Stanier, C. O., and Pandis, S. N.: Coupled Partitioning, Dilution, and Chemical Aging of Semivolatile Organics, Environ. Sci. Technol., 40, 2635–2643, https://doi.org/10.1021/es052297c, 2006.

Donahue, N. M., Epstein, S. A., Pandis, S. N., and Robinson, A. L.: A two-dimensional volatility basis set: 1. organic-aerosol mixing thermodynamics, Atmos. Chem. Phys., 11, 3303–3318, https://doi.org/10.5194/acp-11-3303-2011, 2011.

Donahue, N. M., Kroll, J. H., Pandis, S. N., and Robinson, A. L.: A two-dimensional volatility basis set – Part 2: Diagnostics of organic-aerosol evolution, Atmos. Chem. Phys., 12, 615–634, https://doi.org/10.5194/acp-12-615-2012, 2012.

Eichler, P., Müller, M., D'Anna, B., and Wisthaler, A.: A novel inlet system for online chemical analysis of semi-volatile submicron particulate matter, Atmos. Meas. Tech., 8, 1353–1360, https://doi.org/10.5194/amt-8-1353-2015, 2015.

European Environment Agency: Europe's air quality status 2021, Publications Office, LU, https://data.europa.eu/doi/10.2800/488115 (last access: 18 December 2024), 2022.

Fan, C., Wang, W., Wang, K., Lei, T., Xiang, W., Hou, C., Li, J., Guo, Y., and Ge, M.: Temperature effects on SOA formation of *n*-dodecane reaction initiated by Cl atoms, Atmos. Environ., 346, 121070, https://doi.org/10.1016/j.atmosenv.2025.121070, 2025.

Fan, J. and Zhang, R.: Density Functional Theory Study on OH-Initiated Atmospheric Oxidation of *m*-Xylene, J. Phys. Chem. A, 112, 4314–4323, https://doi.org/10.1021/jp077648j, 2008.

Fang, H., Luo, S., Huang, X., Fu, X., Xiao, S., Zeng, J., Wang, J., Zhang, Y., and Wang, X.: Ambient naphthalene and methylnaphthalenes observed at an urban site in the Pearl River Delta region: Sources and contributions to secondary organic aerosol, Atmos. Environ., 252, 118295, https://doi.org/10.1016/j.atmosenv.2021.118295, 2021.

Fang, H., Wang, W., Xu, H., Huang, Y., Jiang, H., Wu, T., Li, J., Zha, S., Zhang, J., Zhou, R., and Wang, X.: Sources and secondary transformation potentials of aromatic hydrocarbons observed in a medium-sized city in yangtze river delta region: Emphasis on intermediate-volatility naphthalene, Atmos. Environ., 318, 120239, https://doi.org/10.1016/j.atmosenv.2023.120239, 2024.

Forstner, H. J. L., Flagan, R. C., and Seinfeld, J. H.: Secondary Organic Aerosol from the Photooxidation of Aromatic Hydrocarbons: Molecular Composition, Environ. Sci. Technol., 31, 1345–1358, https://doi.org/10.1021/es9605376, 1997.

Gioumousis, G. and Stevenson, D. P.: Reactions of Gaseous Molecule Ions with Gaseous Molecules. V. Theory, J. Chem. Phys., 29, 294–299, https://doi.org/10.1063/1.1744477, 1958.

Gkatzelis, G. I., Hohaus, T., Tillmann, R., Gensch, I., Müller, M., Eichler, P., Xu, K.-M., Schlag, P., Schmitt, S. H., Yu, Z., Wegener, R., Kaminski, M., Holzinger, R., Wisthaler, A., and Kiendler-Scharr, A.: Gas-to-particle partitioning of major biogenic oxidation products: a study on freshly formed and aged biogenic SOA, Atmos. Chem. Phys., 18, 12969–12989, https://doi.org/10.5194/acp-18-12969-2018, 2018.

Heald, C. L., Jacob, D. J., Park, R. J., Russell, L. M., Huebert, B. J., Seinfeld, J. H., Liao, H., and Weber, R. J.: A large organic aerosol source in the free troposphere missing from current models, Geophys. Res. Lett., 32, 2005GL023831, https://doi.org/10.1029/2005GL023831, 2005.

Healy, R. M., Chen, Y., Kourtchev, I., Kalberer, M., O'Shea, D., and Wenger, J. C.: Rapid Formation of Secondary Organic Aerosol from the Photolysis of 1-Nitronaphthalene: Role of Naphthoxy Radical Self-reaction, Environ. Sci. Technol., 46, 11813–11820, https://doi.org/10.1021/es302841j, 2012.

Henze, D. K., Seinfeld, J. H., Ng, N. L., Kroll, J. H., Fu, T.-M., Jacob, D. J., and Heald, C. L.: Global modeling of secondary organic aerosol formation from aromatic hydrocarbons: high- vs. low-yield pathways, Atmos. Chem. Phys., 8, 2405–2420, https://doi.org/10.5194/acp-8-2405-2008, 2008.

Huang, D. D., Kong, L., Gao, J., Lou, S., Qiao, L., Zhou, M., Ma, Y., Zhu, S., Wang, H., Chen, S., Zeng, L., and Huang, C.: Insights into the formation and properties of secondary organic aerosol at a background site in Yangtze River Delta region of China: Aqueous-phase processing vs. photochemical oxidation, Atmos. Environ., 239, 117716, https://doi.org/10.1016/j.atmosenv.2020.117716, 2020.

Huang, M., Zhang, W., Hao, L., Wang, Z., Zhao, W., Gu, X., and Fang, L.: Low-Molecular Weight and Oligomeric Components in Secondary Organic Aerosol from the Photooxidation of *p*-Xylene, J. Chinese Chemical Soc., 55, 456–463, https://doi.org/10.1002/jccs.200800068, 2008.

Huang, R.-J., Zhang, Y., Bozzetti, C., Ho, K.-F., Cao, J.-J., Han, Y., Daellenbach, K. R., Slowik, J. G., Platt, S. M., Canonaco, F., Zotter, P., Wolf, R., Pieber, S. M., Bruns, E. A., Crippa, M., Ciarelli, G., Piazzalunga, A., Schwikowski, M., Abbaszade, G., Schnelle-Kreis, J., Zimmermann, R., An, Z., Szi-

dat, S., Baltensperger, U., Haddad, I. E., and Prévôt, A. S. H.: High secondary aerosol contribution to particulate pollution during haze events in China, Nature, 514, 218–222, https://doi.org/10.1038/nature13774, 2014.

Ijaz, A., Temime-Roussel, B., Kammer, J., Mao, J., Simpson, W., Law, K. S., and Barbara, D.: In situ measurements of gas-particle partitioning of organic compounds in Fairbanks, Faraday Discuss., 258, 23–39, https://doi.org/10.1039/D4FD00175C, 2024.

Isaacman-VanWertz, G., Yee, L. D., Kreisberg, N. M., Wernis, R., Moss, J. A., Hering, S. V., De Sá, S. S., Martin, S. T., Alexander, M. L., Palm, B. B., Hu, W., Campuzano-Jost, P., Day, D. A., Jimenez, J. L., Riva, M., Surratt, J. D., Viegas, J., Manzi, A., Edgerton, E., Baumann, K., Souza, R., Artaxo, P., and Goldstein, A. H. : Ambient Gas-Particle Partitioning of Tracers for Biogenic Oxidation, Environ. Sci. Technol., 50, 9952–9962, https://doi.org/10.1021/acs.est.6b01674, 2016.

Isaacman-VanWertz, G., Massoli, P., O'Brien, R., Lim, C., Franklin, J. P., Moss, J. A., Hunter, J. F., Nowak, J. B., Canagaratna, M. R., Misztal, P. K., Arata, C., Roscioli, J. R., Herndon, S. T., Onasch, T. B., Lambe, A. T., Jayne, J. T., Su, L., Knopf, D. A., Goldstein, A. H., Worsnop, D. R., and Kroll, J. H.: Chemical evolution of atmospheric organic carbon over multiple generations of oxidation, Nat. Chem., 10, 462–468, https://doi.org/10.1038/s41557-018-0002-2, 2018.

Jang, M. and Kamens, R. M.: Characterization of Secondary Aerosol from the Photooxidation of Toluene in the Presence of NO_x and 1-Propene, Environ. Sci. Technol., 35, 3626–3639, https://doi.org/10.1021/es010676+, 2001.

Jang, M., Czoschke, N. M., Lee, S., and Kamens, R. M.: Heterogeneous Atmospheric Aerosol Production by Acid-Catalyzed Particle-Phase Reactions, Science, New Series, 298, 814–817, https://doi.org/10.1126/science.1075798, 2002.

Jenkin, M. E., Saunders, S. M., Wagner, V., and Pilling, M. J.: Protocol for the development of the Master Chemical Mechanism, MCM v3 (Part B): tropospheric degradation of aromatic volatile organic compounds, Atmos. Chem. Phys., 3, 181–193, https://doi.org/10.5194/acp-3-181-2003, 2003.

Jiang, Z., Grosselin, B., Daële, V., Mellouki, A., and Mu, Y.: Seasonal and diurnal variations of BTEX compounds in the semi-urban environment of Orleans, France, Sci. Total Environ., 574, 1659–1664, https://doi.org/10.1016/j.scitotenv.2016.08.214, 2017.

Jimenez, J. L., Canagaratna, M. R., Donahue, N. M., Prevot, A. S. H., Zhang, Q., Kroll, J. H., DeCarlo, P. F., Allan, J. D., Coe, H., Ng, N. L., Aiken, A. C., Docherty, K. S., Ulbrich, I. M., Grieshop, A. P., Robinson, A. L., Duplissy, J., Smith, J. D., Wilson, K. R., Lanz, V. A., Hueglin, C., Sun, Y. L., Tian, J., Laaksonen, A., Raatikainen, T., Rautiainen, J., Vaattovaara, P., Ehn, M., Kulmala, M., Tomlinson, J. M., Collins, D. R., Cubison, M. J., E., Dunlea, J., Huffman, J. A., Onasch, T. B., Alfarra, M. R., Williams, P. I., Bower, K., Kondo, Y., Schneider, J., Drewnick, F., Borrmann, S., Weimer, S., Demerjian, K., Salcedo, D., Cottrell, L., Griffin, R., Takami, A., Miyoshi, T., Hatakeyama, S., Shimono, A., Sun, J. Y., Zhang, Y. M., Dzepina, K., Kimmel, J. R., Sueper, D., Jayne, J. T., Herndon, S. C., Trimborn, A. M., Williams, L. R., Wood, E. C., Middlebrook, A. M., Kolb, C. E., Baltensperger, U., and Worsnop, D. R.: Evolution of Organic Aerosols in the Atmosphere, Science, 326, 1525–1529, https://doi.org/10.1126/science.1180353, 2009.

Jin, Z.-H., Yu, D., Liu, Y.-X., Tian, Z.-Y., Richter, S., Braun-Unkhoff, M., Naumann, C., and Yang, J.-Z.: An experimental investigation of furfural oxidation and the development of a comprehensive combustion model, Combust. Flame, 226, 200–210, https://doi.org/10.1016/j.combustflame.2020.12.015, 2021.

John, E., Coburn, S., Liu, C., McAughey, J., Mariner, D., McAdam, K. G., Sebestyén, Z., Bakos, I., and Dóbé, S.: Effect of temperature and humidity on the gas–particle partitioning of nicotine in mainstream cigarette smoke: A diffusion denuder study, J. Aerosol Sci., 117, 100–117, https://doi.org/10.1016/j.jaerosci.2017.12.015, 2018.

Kamens, R. M., Zhang, H., Chen, E. H., Zhou, Y., Parikh, H. M., Wilson, R. L., Galloway, K. E., and Rosen, E. P.: Secondary organic aerosol formation from toluene in an atmospheric hydrocarbon mixture: Water and particle seed effects, Atmos. Environ., 45, 2324–2334, https://doi.org/10.1016/j.atmosenv.2010.11.007, 2011.

Kang, E., Root, M. J., Toohey, D. W., and Brune, W. H.: Introducing the concept of Potential Aerosol Mass (PAM), Atmos. Chem. Phys., 7, 5727–5744, https://doi.org/10.5194/acp-7-5727-2007, 2007.

Kautzman, K. E., Surratt, J. D., Chan, M. N., Chan, A. W. H., Hersey, S. P., Chhabra, P. S., Dalleska, N. F., Wennberg, P. O., Flagan, R. C., and Seinfeld, J. H.: Chemical Composition of Gas- and Aerosol-Phase Products from the Photooxidation of Naphthalene, J. Phys. Chem. A, 114, 913–934, https://doi.org/10.1021/jp908530s, 2010.

Kim, D.-Y., Soda, S., Kendo, A., and Oh, J.-H.: Atmospheric Photochemistry in Low-and High-NO_x Regimes, Journal of Environmental Science International, 16, 1–8, https://doi.org/10.5322/JES.2007.16.1.001, 2007.

Kleindienst, T. E., Jaoui, M., Lewandowski, M., Offenberg, J. H., and Docherty, K. S.: The formation of SOA and chemical tracer compounds from the photooxidation of naphthalene and its methyl analogs in the presence and absence of nitrogen oxides, Atmos. Chem. Phys., 12, 8711–8726, https://doi.org/10.5194/acp-12-8711-2012, 2012.

Klodt, A. L., Aiona, P. K., MacMillan, A. C., Ji (Julie) Lee, H., Zhang, X., Helgestad, T., Novak, G. A., Lin, P., Laskin, J., Laskin, A., Bertram, T. H., Cappa, C. D., and Nizkorodov, S. A.: Effect of relative humidity, NO_x, and ammonia on the physical properties of naphthalene secondary organic aerosols, Environ. Sci.: Atmos., 3, 991–1007, https://doi.org/10.1039/D3EA00033H, 2023.

Kostenidou, E., Marques, B., Temime-Roussel, B., Liu, Y., Vansevenant, B., Sartelet, K., and D'Anna, B.: Secondary organic aerosol formed by Euro 5 gasoline vehicle emissions: chemical composition and gas-to-particle phase partitioning, Atmos. Chem. Phys., 24, 2705–2729, https://doi.org/10.5194/acp-24-2705-2024, 2024.

Kroll, J. H. and Seinfeld, J. H.: Chemistry of secondary organic aerosol: Formation and evolution of low-volatility organics in the atmosphere, Atmos. Environ., 42, 3593–3624, https://doi.org/10.1016/j.atmosenv.2008.01.003, 2008.

Kroll, J. H., Donahue, N. M., Jimenez, J. L., Kessler, S. H., Canagaratna, M. R., Wilson, K. R., Altieri, K. E., Mazzoleni, L. R., Wozniak, A. S., Bluhm, H., Mysak, E. R., Smith, J. D., Kolb, C. E., and Worsnop, D. R.: Carbon oxidation state as a metric for describing the chemistry of atmospheric organic aerosol,

Nat. Chem., 3, 133–139, https://doi.org/10.1038/nchem.948, 2011.

La, Y. S., Camredon, M., Ziemann, P. J., Valorso, R., Matsunaga, A., Lannuque, V., Lee-Taylor, J., Hodzic, A., Madronich, S., and Aumont, B.: Impact of chamber wall loss of gaseous organic compounds on secondary organic aerosol formation: explicit modeling of SOA formation from alkane and alkene oxidation, Atmos. Chem. Phys., 16, 1417–1431, https://doi.org/10.5194/acp-16-1417-2016, 2016.

Lambe, A. T., Chhabra, P. S., Onasch, T. B., Brune, W. H., Hunter, J. F., Kroll, J. H., Cummings, M. J., Brogan, J. F., Parmar, Y., Worsnop, D. R., Kolb, C. E., and Davidovits, P.: Effect of oxidant concentration, exposure time, and seed particles on secondary organic aerosol chemical composition and yield, Atmos. Chem. Phys., 15, 3063–3075, https://doi.org/10.5194/acp-15-3063-2015, 2015.

Lamkaddam, H., Gratien, A., Pangui, E., Cazaunau, M., Picquet-Varrault, B., and Doussin, J.-F.: High-NO_x Photooxidation of *n*-Dodecane: Temperature Dependence of SOA Formation, Environ. Sci. Technol., 51, 192–201, https://doi.org/10.1021/acs.est.6b03821, 2017.

Langevin, P.: Une formule fondamentale de théorie cinétique, Ann. Chim. Phys., 1905, 269–300, 1950.

Lannuque, V. and Sartelet, K.: Development of a detailed gaseous oxidation scheme of naphthalene for secondary organic aerosol (SOA) formation and speciation, Atmos. Chem. Phys., 24, 8589–8606, https://doi.org/10.5194/acp-24-8589-2024, 2024.

Lannuque, V., Camredon, M., Couvidat, F., Hodzic, A., Valorso, R., Madronich, S., Bessagnet, B., and Aumont, B.: Exploration of the influence of environmental conditions on secondary organic aerosol formation and organic species properties using explicit simulations: development of the VBS-GECKO parameterization, Atmos. Chem. Phys., 18, 13411–13428, https://doi.org/10.5194/acp-18-13411-2018, 2018.

Lannuque, V., D'Anna, B., Kostenidou, E., Couvidat, F., Martinez-Valiente, A., Eichler, P., Wisthaler, A., Müller, M., Temime-Roussel, B., Valorso, R., and Sartelet, K.: Gas–particle partitioning of toluene oxidation products: an experimental and modeling study, Atmos. Chem. Phys., 23, 15537–15560, https://doi.org/10.5194/acp-23-15537-2023, 2023.

Lee, J. Y. and Lane, D. A.: Unique products from the reaction of naphthalene with the hydroxyl radical, Atmos. Environ., 43, 4886–4893, https://doi.org/10.1016/j.atmosenv.2009.07.018, 2009.

Leglise, J., Müller, M., Piel, F., Otto, T., and Wisthaler, A.: Bulk Organic Aerosol Analysis by Proton-Transfer-Reaction Mass Spectrometry: An Improved Methodology for the Determination of Total Organic Mass, O : C and H : C Elemental Ratios, and the Average Molecular Formula, Anal. Chem., 91, 12619–12624, https://doi.org/10.1021/acs.analchem.9b02949, 2019.

Li, J., Wang, W., Li, K., Zhang, W., Peng, C., Zhou, L., Shi, B., Chen, Y., Liu, M., Li, H., and Ge, M.: Temperature effects on optical properties and chemical composition of secondary organic aerosol derived from *n*-dodecane, Atmos. Chem. Phys., 20, 8123–8137, https://doi.org/10.5194/acp-20-8123-2020, 2020.

Li, K., Wang, W., Ge, M., Li, J., and Wang, D.: Optical properties of secondary organic aerosols generated by photooxidation of aromatic hydrocarbons, Sci. Rep., 4, 4922, https://doi.org/10.1038/srep04922, 2014.

Li, K., Li, J., Liggio, J., Wang, W., Ge, M., Liu, Q., Guo, Y., Tong, S., Li, J., Peng, C., Jing, B., Wang, D., and Fu, P.: Enhanced Light Scattering of Secondary Organic Aerosols by Multiphase Reactions, Environ. Sci. Technol., 51, 1285–1292, https://doi.org/10.1021/acs.est.6b03229, 2017.

Li, K., Li, J., Wang, W., Li, J., Peng, C., Wang, D., and Ge, M.: Effects of Gas-Particle Partitioning on Refractive Index and Chemical Composition of *m* -Xylene Secondary Organic Aerosol, J. Phys. Chem. A, 122, 3250–3260, https://doi.org/10.1021/acs.jpca.7b12792, 2018.

Li, L., Thomsen, D., Wu, C., Priestley, M., Iversen, E. M., Tygesen Skønager, J., Luo, Y., Ehn, M., Roldin, P., Pedersen, H. B., Bilde, M., Glasius, M., and Hallquist, M.: Gas-to-Particle Partitioning of Products from Ozonolysis of Δ^3-Carene and the Effect of Temperature and Relative Humidity, J. Phys. Chem. A, 128, 918–928, https://doi.org/10.1021/acs.jpca.3c07316, 2024.

Li, Y., Zhao, J., Gomez-Hernandez, M., Lavallee, M., Johnson, N. M., and Zhang, R.: Functionality-based formation of secondary organic aerosol from *m*-xylene photooxidation, Atmos. Chem. Phys., 22, 9843–9857, https://doi.org/10.5194/acp-22-9843-2022, 2022.

Li, Z., Schwier, A. N., Sareen, N., and McNeill, V. F.: Reactive processing of formaldehyde and acetaldehyde in aqueous aerosol mimics: surface tension depression and secondary organic products, Atmos. Chem. Phys., 11, 11617–11629, https://doi.org/10.5194/acp-11-11617-2011, 2011.

Li, Z., Tikkanen, O.-P., Buchholz, A., Hao, L., Kari, E., Yli-Juuti, T., and Virtanen, A.: Effect of Decreased Temperature on the Evaporation of α-Pinene Secondary Organic Aerosol Particles, ACS Earth Space Chem., 3, 2775–2785, https://doi.org/10.1021/acsearthspacechem.9b00240, 2019.

Liang, Y., Wernis, R. A., Kristensen, K., Kreisberg, N. M., Croteau, P. L., Herndon, S. C., Chan, A. W. H., Ng, N. L., and Goldstein, A. H.: Gas–particle partitioning of semivolatile organic compounds when wildfire smoke comes to town, Atmos. Chem. Phys., 23, 12441–12454, https://doi.org/10.5194/acp-23-12441-2023, 2023.

Liu, J., Zhu, S., Guo, T., Jia, B., Xu, L., Chen, J., and Cheng, P.: Smog chamber study of secondary organic aerosol formation from gas- and particle-phase naphthalene ozonolysis, Atmos. Environ., 294, 119490, https://doi.org/10.1016/j.atmosenv.2022.119490, 2023.

Liu, K., Hua, S., and Song, L.: $PM_{2.5}$ Exposure and Asthma Development: The Key Role of Oxidative Stress, Oxid. Med. Cell. Longev., 2022, 1–12, https://doi.org/10.1155/2022/3618806, 2022a.

Liu, M. and Matsui, H.: Impacts of Climate Change on Particulate Matter (PM), in: Handbook of Air Quality and Climate Change, edited by: Akimoto, H. and Tanimoto, H., Springer Nature, Singapore, 1–18, https://doi.org/10.1007/978-981-15-2527-8_39-1, 2020.

Liu, M., Bi, J., and Ma, Z.: Visibility-Based $PM_{2.5}$ Concentrations in China: 1957–1964 and 1973–2014, Environ. Sci. Technol., 51, 13161–13169, https://doi.org/10.1021/acs.est.7b03468, 2017.

Liu, Q., Huang, D. D., Lambe, A. T., Lou, S., Zeng, L., Wu, Y., Huang, C., Tao, S., Cheng, X., Chen, Q., Hoi, K. I., Wang, H., Mok, K. M., Huang, C., and Li, Y. J.: A Comprehensive Characterization of Empirical Parameterizations for OH Exposure in the Aerodyne Potential Aerosol Mass

Oxidation Flow Reactor (PAM-OFR), EGUsphere [preprint], https://doi.org/10.5194/egusphere-2024-2721, 2024.

Liu, S., Wang, Y., Xu, X., and Wang, G.: Effects of NO_2 and RH on secondary organic aerosol formation and light absorption from OH oxidation of *o*-xylene, Chemosphere, 308, 136541, https://doi.org/10.1016/j.chemosphere.2022.136541, 2022b.

Liu, X., Day, D. A., Krechmer, J. E., Ziemann, P. J., and Jimenez, J. L.: Determining Activity Coefficients of SOA from Isothermal Evaporation in a Laboratory Chamber, Environ. Sci. Tech. Let., 8, 212–217, https://doi.org/10.1021/acs.estlett.0c00888, 2021.

Loeffler, K. W., Koehler, C. A., Paul, N. M., and De Haan, D. O.: Oligomer Formation in Evaporating Aqueous Glyoxal and Methyl Glyoxal Solutions, Environ. Sci. Technol., 40, 6318–6323, https://doi.org/10.1021/es060810w, 2006.

Loza, C. L., Chhabra, P. S., Yee, L. D., Craven, J. S., Flagan, R. C., and Seinfeld, J. H.: Chemical aging of *m*-xylene secondary organic aerosol: laboratory chamber study, Atmos. Chem. Phys., 12, 151–167, https://doi.org/10.5194/acp-12-151-2012, 2012.

Lu, H., Huang, Q., Li, J., Ying, Q., Wang, H., Guo, S., Qin, M., and Hu, J.: Simulation of Regional Secondary Organic Aerosol Formation From Monocyclic Aromatic Hydrocarbons Using a Near-Explicit Chemical Mechanism Constrained by Chamber Experiments, JGR Atmospheres, 129, e2023JD040690, https://doi.org/10.1029/2023JD040690, 2024.

Lu, R., Zhou, P., Ma, F., Zhao, Q., Peng, X., Chen, J., and Xie, H.-B.: Multi-generation oxidation mechanism of M-xylene: Unexpected implications for secondary organic aerosol formation, Atmos. Environ., 327, 120511, https://doi.org/10.1016/j.atmosenv.2024.120511, 2024.

Mao, J., Ren, X., Brune, W. H., Olson, J. R., Crawford, J. H., Fried, A., Huey, L. G., Cohen, R. C., Heikes, B., Singh, H. B., Blake, D. R., Sachse, G. W., Diskin, G. S., Hall, S. R., and Shetter, R. E.: Airborne measurement of OH reactivity during INTEX-B, Atmos. Chem. Phys., 9, 163–173, https://doi.org/10.5194/acp-9-163-2009, 2009.

McWhinney, R. D., Zhou, S., and Abbatt, J. P. D.: Naphthalene SOA: redox activity and naphthoquinone gas–particle partitioning, Atmos. Chem. Phys., 13, 9731–9744, https://doi.org/10.5194/acp-13-9731-2013, 2013.

Meng, X., Wu, Z., Chen, J., Qiu, Y., Zong, T., Song, M., Lee, J., and Hu, M.: Particle phase state and aerosol liquid water greatly impact secondary aerosol formation: insights into phase transition and its role in haze events, Atmos. Chem. Phys., 24, 2399–2414, https://doi.org/10.5194/acp-24-2399-2024, 2024.

Meredith, L. K., Ledford, S. M., Riemer, K., Geffre, P., Graves, K., Honeker, L. K., LeBauer, D., Tfaily, M. M., and Krechmer, J.: Automating methods for estimating metabolite volatility, Front. Microbiol., 14, 1267234, https://doi.org/10.3389/fmicb.2023.1267234, 2023.

Molina, M. J., Zhang, R., Broekhuizen, K., Lei, W., Navarro, R., and Molina, L. T.: Experimental Study of Intermediates from OH-Initiated Reactions of Toluene, J. Am. Chem. Soc., 121, 10225–10226, https://doi.org/10.1021/ja992461u, 1999.

Montero-Montoya, R., López-Vargas, R., and Arellano-Aguilar, O.: Volatile Organic Compounds in Air: Sources, Distribution, Exposure and Associated Illnesses in Children, Ann. Glob. Health, 84, 225–238, https://doi.org/10.29024/aogh.910, 2018.

Müller, M., Graus, M., Wisthaler, A., Hansel, A., Metzger, A., Dommen, J., and Baltensperger, U.: Analysis of high mass resolution PTR-TOF mass spectra from 1,3,5-trimethylbenzene (TMB) environmental chamber experiments, Atmos. Chem. Phys., 12, 829–843, https://doi.org/10.5194/acp-12-829-2012, 2012.

Müller, M., Mikoviny, T., Jud, W., D'Anna, B., and Wisthaler, A.: A new software tool for the analysis of high resolution PTR-TOF mass spectra, Chemometr. Intell. Lab., 127, 158–165, https://doi.org/10.1016/j.chemolab.2013.06.011, 2013.

Müller, M., Eichler, P., D'Anna, B., Tan, W., and Wisthaler, A.: Direct Sampling and Analysis of Atmospheric Particulate Organic Matter by Proton-Transfer-Reaction Mass Spectrometry, Anal. Chem., 89, 10889–10897, https://doi.org/10.1021/acs.analchem.7b02582, 2017.

Murphy, B. N., Donahue, N. M., Fountoukis, C., Dall'Osto, M., O'Dowd, C., Kiendler-Scharr, A., and Pandis, S. N.: Functionalization and fragmentation during ambient organic aerosol aging: application of the 2-D volatility basis set to field studies, Atmos. Chem. Phys., 12, 10797–10816, https://doi.org/10.5194/acp-12-10797-2012, 2012.

NARSTO and Electric Power Research Institute: An assessment of tropospheric ozone pollution: a North American perspective, EPRI, https://catalog.libraries.psu.edu/catalog/2213430 (last access: 9 April 2024), 2000.

Ng, N. L., Kroll, J. H., Chan, A. W. H., Chhabra, P. S., Flagan, R. C., and Seinfeld, J. H.: Secondary organic aerosol formation from *m*-xylene, toluene, and benzene, Atmos. Chem. Phys., 7, 3909–3922, https://doi.org/10.5194/acp-7-3909-2007, 2007.

Ng, N. L., Kroll, J. H., Chan, A. W. H., Chhabra, P. S., Flagan, R. C., and Seinfeld, J. H.: Secondary organic aerosol formation from m-xylene, toluene, and benzene, Atmos. Chem. Phys., 7, 3909– 3922, https://doi.org/10.5194/acp-7-3909-2007, 2007.

Nie, W., Yan, C., Huang, D., Wang, Z., Liu, Y., Qiao, X., Guo, Y., Tian, L., Zheng, P., Xu, Z., Li, Y., Xu, Z., Qi, X., Sun, P., Wang, J., Zheng, F., Li, X., Yin, R., Dallenbach, K., Bianchi, F., Petäjä, T., Zhang, Y., Wang, M., Schervish, M., Wang, S., Qiao, L., Wang, Q., Zhou, M., Wang, H., Yu, C., Yao, D., Guo, H., Ye, P., Lee, S., Li, Y., Liu, Y., Chi, X., Kerminen, V., Ehn, M., Donahue, N., Wang, T., Huang, C., Kulmala, M., Worsnop, D., Jiang, J., and Ding, A.: Secondary organic aerosol formed by condensing anthropogenic vapours over China's megacities, Nat Geosci., 15, 255–261, https://doi.org/10.1038/s41561-022-00922-5, 2022.

Nishino, N., Arey, J., and Atkinson, R.: Formation and Reactions of 2-Formylcinnamaldehyde in the OH Radical-Initiated Reaction of Naphthalene, Environ. Sci. Technol., 43, 1349–1353, https://doi.org/10.1021/es802477s, 2009.

Nozière, B., Dziedzic, P., and Córdova, A.: Inorganic ammonium salts and carbonate salts are efficient catalysts for aldol condensation in atmospheric aerosols, Phys. Chem. Chem. Phys., 12, 3864, https://doi.org/10.1039/b924443c, 2010.

Odum, J. R., Hoffmann, T., Bowman, F., Collins, D., Flagan, R. C., and Seinfeld, J. H.: Gas/Particle Partitioning and Secondary Organic Aerosol Yields, Environ. Sci. Technol., 30, 2580–2585, https://doi.org/10.1021/es950943+, 1996.

Odum, J. R., Jungkamp, T. P. W., Griffin, R. J., Forstner, H. J. L., Flagan, R. C., and Seinfeld, J. H.: Aromatics, Reformulated Gasoline, and Atmospheric Organic Aerosol

Formation, Environ. Sci. Technol., 31, 1890–1897, https://doi.org/10.1021/es960535L, 1997.

O'Meara, S., Booth, A. M., Barley, M. H., Topping, D., and McFiggans, G.: An assessment of vapour pressure estimation methods, Phys. Chem. Chem. Phys., 16, 19453–19469, https://doi.org/10.1039/C4CP00857J, 2014.

Pan, S. and Wang, L.: Atmospheric Oxidation Mechanism of *m*-Xylene Initiated by OH Radical, J. Phys. Chem. A, 118, 10778–10787, https://doi.org/10.1021/jp506815v, 2014.

Pang, X.: Biogenic volatile organic compound analyses by PTR-TOF-MS: Calibration, humidity effect and reduced electric field dependency, J. Environ. Sci., 32, 196–206, https://doi.org/10.1016/j.jes.2015.01.013, 2015.

Pankow, J. F. and Asher, W. E.: SIMPOL.1: a simple group contribution method for predicting vapor pressures and enthalpies of vaporization of multifunctional organic compounds, Atmos. Chem. Phys., 8, 2773–2796, https://doi.org/10.5194/acp-8-2773-2008, 2008.

Peng, Y., Wang, H., Gao, Y., Jing, S., Zhu, S., Huang, D., Hao, P., Lou, S., Cheng, T., Huang, C., and Zhang, X.: Real-time measurement of phase partitioning of organic compounds using a proton-transfer-reaction time-of-flight mass spectrometer coupled to a CHARON inlet, Atmos. Meas. Tech., 16, 15–28, https://doi.org/10.5194/amt-16-15-2023, 2023.

Peng, Z. and Jimenez, J. L.: Radical chemistry in oxidation flow reactors for atmospheric chemistry research, Chem. Soc. Rev., 49, 2570–2616, https://doi.org/10.1039/C9CS00766K, 2020.

Peräkylä, O., Riva, M., Heikkinen, L., Quéléver, L., Roldin, P., and Ehn, M.: Experimental investigation into the volatilities of highly oxygenated organic molecules (HOMs) , Atmos. Chem. Phys., 20, 649–669, https://doi.org/10.5194/acp-20-649-2020, 2020.

Piel, F., Müller, M., Winkler, K., Skytte af Sätra, J., and Wisthaler, A.: Introducing the extended volatility range proton-transfer-reaction mass spectrometer (EVR PTR-MS), Atmos. Meas. Tech., 14, 1355–1363, https://doi.org/10.5194/amt-14-1355-2021, 2021.

Price, D. J., Kacarab, M., Cocker, D. R., Purvis-Roberts, K. L., and Silva, P. J.: Effects of temperature on the formation of secondary organic aerosol from amine precursors, Aerosol Sci. Tech., 50, 1216–1226, https://doi.org/10.1080/02786826.2016.1236182, 2016.

Qi, L., Nakao, S., Tang, P., and Cocker III, D. R.: Temperature effect on physical and chemical properties of secondary organic aerosol from *m*-xylene photooxidation, Atmos. Chem. Phys., 10, 3847–3854, https://doi.org/10.5194/acp-10-3847-2010, 2010.

Qi, X., Zhu, S., Zhu, C., Hu, J., Lou, S., Xu, L., Dong, J., and Cheng, P.: Smog chamber study of the effects of NO_x and NH3 on the formation of secondary organic aerosols and optical properties from photo-oxidation of toluene, Sci. Total Environ., 727, 138632, https://doi.org/10.1016/j.scitotenv.2020.138632, 2020.

Qu, X., Zhang, Q., and Wang, W.: Mechanism for OH-initiated photooxidation of naphthalene in the presence of O_2 and NO_x: A DFT study, Chem. Phys. Lett., 429, 77–85, https://doi.org/10.1016/j.cplett.2006.08.036, 2006.

Riemer, K.: volcalc: Calculate Volatility of Chemical Compounds, Zenodo [code], https://doi.org/10.5281/ZENODO.8015155, 2023.

Riva, M.: Caractérisation d'une nouvelle voie de formation d'aérosols organiques secondaires (AOS) dans l'atmosphère: Rôle des précurseurs polyaromatiques, Université Bordeaux 1, https://theses.hal.science/file/index/docid/952636/filename/RIVA_MATTHIEU_2013.pdf (last access: 5 May 2025), 2013.

Rutter, A. P. and Schauer, J. J.: The effect of temperature on the gas–particle partitioning of reactive mercury in atmospheric aerosols, Atmos. Environ., 41, 8647–8657, https://doi.org/10.1016/j.atmosenv.2007.07.024, 2007.

Salvador, C. M., Chou, C. C.-K., Cheung, H.-C., Ho, T.-T., Tsai, C.-Y., Tsao, T.-M., Tsai, M.-J., and Su, T.-C.: Measurements of submicron organonitrate particles: Implications for the impacts of NO_x pollution in a subtropical forest, Atmos. Res., 245, 105080, https://doi.org/10.1016/j.atmosres.2020.105080, 2020.

Sareen, N., Schwier, A. N., Shapiro, E. L., Mitroo, D., and McNeill, V. F.: Secondary organic material formed by methylglyoxal in aqueous aerosol mimics, Atmos. Chem. Phys., 10, 997–1016, https://doi.org/10.5194/acp-10-997-2010, 2010.

Sarrafzadeh, M., Wildt, J., Pullinen, I., Springer, M., Kleist, E., Tillmann, R., Schmitt, S. H., Wu, C., Mentel, T. F., Zhao, D., Hastie, D. R., and Kiendler-Scharr, A.: Impact of NO_x and OH on secondary organic aerosol formation from β-pinene photooxidation, Atmos. Chem. Phys., 16, 11237–11248, https://doi.org/10.5194/acp-16-11237-2016, 2016.

Sasaki, J., Aschmann, S. M., Kwok, E. S. C., Atkinson, R., and Arey, J.: Products of the Gas-Phase OH and NO_3 Radical-Initiated Reactions of Naphthalene, Environ. Sci. Technol., 31, 3173–3179, https://doi.org/10.1021/es9701523, 1997.

Sato, K., Hatakeyama, S., and Imamura, T.: Secondary Organic Aerosol Formation during the Photooxidation of Toluene: NO_x Dependence of Chemical Composition, J. Phys. Chem. A, 111, 9796–9808, https://doi.org/10.1021/jp071419f, 2007.

Sato, K., Ikemori, F., Ramasamy, S., Iijima, A., Kumagai, K., Fushimi, A., Fujitani, Y., Chatani, S., Tanabe, K., Takami, A., Tago, H., Saito, Y., Saito, S., Hoshi, J., and Morino, Y.: Formation of secondary organic aerosol tracers from anthropogenic and biogenic volatile organic compounds under varied NO_x and oxidant conditions, Atmos. Environ., 14, 100169, https://doi.org/10.1016/j.aeaoa.2022.100169, 2022.

Schwantes, R. H., Charan, S. M., Bates, K. H., Huang, Y., Nguyen, T. B., Mai, H., Kong, W., Flagan, R. C., and Seinfeld, J. H.: Low-volatility compounds contribute significantly to isoprene secondary organic aerosol (SOA) under high-NO_x conditions, Atmos. Chem. Phys., 19, 7255–7278, https://doi.org/10.5194/acp-19-7255-2019, 2019.

Seinfeld, J. H. and Pandis, S. N.: Atmospheric chemistry and physics: from air pollution to climate change, Third edition., John Wiley & Sons, Inc. Hoboken, New Jersey, ISBN 978-1-118-94740-1, 2016.

Sekimoto, K., Li, S.-M., Yuan, B., Koss, A., Coggon, M., Warneke, C., and De Gouw, J.: Calculation of the sensitivity of proton-transfer-reaction mass spectrometry (PTR-MS) for organic trace gases using molecular properties, Int. J. Mass Spectrom., 421, 71–94, https://doi.org/10.1016/j.ijms.2017.04.006, 2017.

Shapiro, E. L., Szprengiel, J., Sareen, N., Jen, C. N., Giordano, M. R., and McNeill, V. F.: Light-absorbing secondary organic material formed by glyoxal in aqueous aerosol mimics, Atmos. Chem. Phys., 9, 2289–2300, https://doi.org/10.5194/acp-9-2289-2009, 2009.

Shi, D., Liu, J., Wang, Y., Xu, L., Guo, T., Jia, B., and Cheng, P.: Secondary organic aerosol formation from cis-3-hexen-1-ol/NO_x photo-oxidation: The roles of cis-3-hexen-1-ol concentration, illumination intensity, NO_x and NH3, Atmos. Environ., 278, 119090, https://doi.org/10.1016/j.atmosenv.2022.119090, 2022.

Shrivastava, M., Cappa, C. D., Fan, J., Goldstein, A. H., Guenther, A. B., Jimenez, J. L., Kuang, C., Laskin, A., Martin, S. T., Ng, N. L., Petaja, T., Pierce, J. R., Rasch, P. J., Roldin, P., Seinfeld, J. H., Shilling, J., Smith, J. N., Thornton, J. A., Volkamer, R., Wang, J., Worsnop, D. R., Zaveri, R. A., Zelenyuk, A., and Zhang, Q.: Recent advances in understanding secondary organic aerosol: Implications for global climate forcing, Rev. Geophys., 55, 509–559, https://doi.org/10.1002/2016RG000540, 2017.

Singh, K. and Tripathi, D.: Particulate Matter and Human Health, in: Environmental Health, edited by: Otsuki, T., IntechOpen, https://doi.org/10.5772/intechopen.100550, 2021.

Song, C., Na, K., and Cocker, D. R.: Impact of the Hydrocarbon to NO_x Ratio on Secondary Organic Aerosol Formation, Environ. Sci. Technol., 39, 3143–3149, https://doi.org/10.1021/es0493244, 2005.

Song, C., Na, K., Warren, B., Malloy, Q., and Cocker, D. R.: Secondary Organic Aerosol Formation from *m*-Xylene in the Absence of NO_x, Environ. Sci. Technol., 41, 7409–7416, https://doi.org/10.1021/es070429r, 2007.

Song, C., He, J., Wu, L., Jin, T., Chen, X., Li, R., Ren, P., Zhang, L., and Mao, H.: Health burden attributable to ambient $PM_{2.5}$ in China, Environ. Pollut., 223, 575–586, https://doi.org/10.1016/j.envpol.2017.01.060, 2017.

Srivastava, D., Vu, T. V., Tong, S., Shi, Z., and Harrison, R. M.: Formation of secondary organic aerosols from anthropogenic precursors in laboratory studies, npj Clim. Atmos. Sci., 5, 22, https://doi.org/10.1038/s41612-022-00238-6, 2022.

Srivastava, D., Li, W., Tong, S., Shi, Z., and Harrison, R. M.: Characterization of products formed from the oxidation of toluene and *m*-xylene with varying NO_x and OH exposure, Chemosphere, 334, 139002, https://doi.org/10.1016/j.chemosphere.2023.139002, 2023.

Stark, H., Yatavelli, R. L. N., Thompson, S. L., Kang, H., Krechmer, J. E., Kimmel, J. R., Palm, B. B., Hu, W., Hayes, P. L., Day, D. A., Campuzano-Jost, P., Canagaratna, M. R., Jayne, J. T., Worsnop, D. R., and Jimenez, J. L.: Impact of Thermal Decomposition on Thermal Desorption Instruments: Advantage of Thermogram Analysis for Quantifying Volatility Distributions of Organic Species, Environ. Sci. Technol., 51, 8491–8500, https://doi.org/10.1021/acs.est.7b00160, 2017.

Su, T. and Chesnavich, W. J.: Parametrization of the ion–polar molecule collision rate constant by trajectory calculations, J. Chem. Phys., 76, 5183–5185, https://doi.org/10.1063/1.442828, 1982.

Svendby, T. M., Lazaridis, M., and Tørseth, K.: Temperature dependent secondary organic aerosol formation from terpenes and aromatics, J. Atmos. Chem., 59, 25–46, https://doi.org/10.1007/s10874-007-9093-7, 2008.

Takekawa, H., Minoura, H., and Yamazaki, S.: Temperature dependence of secondary organic aerosol formation by photo-oxidation of hydrocarbons, Atmos. Environ., 37, 3413–3424, https://doi.org/10.1016/S1352-2310(03)00359-5, 2003.

Tani, A., Hayward, S., and Hewitt, C. N.: Measurement of monoterpenes and related compounds by proton transfer reaction-mass spectrometry (PTR-MS), Int. J. Mass Spectrom., 223–224, 561–578, https://doi.org/10.1016/S1387-3806(02)00880-1, 2003.

Thangavel, P., Park, D., and Lee, Y.-C.: Recent Insights into Particulate Matter ($PM_{2.5}$)-Mediated Toxicity in Humans: An Overview, IJERPH, 19, 7511, https://doi.org/10.3390/ijerph19127511, 2022.

Tian, L., Huang, D. D., Wang, Q., Zhu, S., Wang, Q., Yan, C., Nie, W., Wang, Z., Qiao, L., Liu, Y., Qiao, X., Guo, Y., Zheng, P., Jing, S., Lou, S., Wang, H., Yu, J. Z., Huang, C., and Li, Y. J.: Underestimated Contribution of Heavy Aromatics to Secondary Organic Aerosol Revealed by Comparative Assessments Using New and Traditional Methods, ACS Earth Space Chem., 7, 110–119, https://doi.org/10.1021/acsearthspacechem.2c00252, 2023.

Tomaz, S.: Etude des composés polyaromatiques dans l'atmosphère: caractérisation moléculaire et processus réactionnels en lien avec l'aérosol organique, Université de Lille, https://theses.hal.science/tel-01290454/ (last access: 19 December 2024), 2015.

Virtanen, A., Joutsensaari, J., Koop, T., Kannosto, J., Yli-Pirilä, P., Leskinen, J., Mäkelä, J. M., Holopainen, J. K., Pöschl, U., Kulmala, M., Worsnop, D. R., and Laaksonen, A.: An amorphous solid state of biogenic secondary organic aerosol particles, Nature, 467, 824–827, https://doi.org/10.1038/nature09455, 2010.

Volkamer, R., Jimenez, J. L., San Martini, F., Dzepina, K., Zhang, Q., Salcedo, D., Molina, L. T., Worsnop, D. R., and Molina, M. J.: Secondary organic aerosol formation from anthropogenic air pollution: Rapid and higher than expected, Geophys. Res. Lett., 33, 2006GL026899, https://doi.org/10.1029/2006GL026899, 2006.

Wang, L., Atkinson, R., and Arey, J.: Dicarbonyl Products of the OH Radical-Initiated Reactions of Naphthalene and the C_1- and C_2-Alkylnaphthalenes, Environ. Sci. Technol., 41, 2803–2810, https://doi.org/10.1021/es0628102, 2007.

Warren, B., Austin, R. L., and Cocker, D. R.: Temperature dependence of secondary organic aerosol, Atmos. Environ., 43, 3548–3555, https://doi.org/10.1016/j.atmosenv.2009.04.011, 2009.

Wei, W., Mandin, C., Blanchard, O., Mercier, F., Pelletier, M., Le Bot, B., Glorennec, P., and Ramalho, O.: Temperature dependence of the particle/gas partition coefficient: An application to predict indoor gas-phase concentrations of semi-volatile organic compounds, Sci. Total Environ., 563–564, 506–512, https://doi.org/10.1016/j.scitotenv.2016.04.106, 2016.

Wu, K., Duan, M., Zhou, J., Zhou, Z., Tan, Q., Song, D., Lu, C., and Deng, Y.: Sources Profiles of Anthropogenic Volatile Organic Compounds from Typical Solvent Used in Chengdu, China, J. Environ. Eng., 146, 05020006, https://doi.org/10.1061/(ASCE)EE.1943-7870.0001739, 2020.

Xu, J., Griffin, R. J., Liu, Y., Nakao, S., and Cocker, D. R.: Simulated impact of NO_x on SOA formation from oxidation of toluene and *m*-xylene, Atmos. Environ., 101, 217–225, https://doi.org/10.1016/j.atmosenv.2014.11.008, 2015.

Xu, L., Kollman, M. S., Song, C., Shilling, J. E., and Ng, N. L.: Effects of NO_x on the Volatility of Secondary Organic Aerosol from Isoprene Photooxidation, Environ. Sci. Technol., 48, 2253–2262, https://doi.org/10.1021/es404842g, 2014.

Xuan, L., Ma, Y., Xing, Y., Meng, Q., Song, J., Chen, T., Wang, H., Wang, P., Zhang, Y., and Gao, P.: Source, temporal variation

and health risk of volatile organic compounds (VOCs) from urban traffic in harbin, China, Environ. Pollut., 270, 116074, https://doi.org/10.1016/j.envpol.2020.116074, 2021.

Yamasaki, H., Kuwata, K., and Miyamoto, H.: Effects of ambient temperature on aspects of airborne polycyclic aromatic hydrocarbons, Environ. Sci. Technol., 16, 189–194, https://doi.org/10.1021/es00098a003, 1982.

Ye, F., Li, J., Gao, Y., Wang, H., An, J., Huang, C., Guo, S., Lu, K., Gong, K., Zhang, H., Qin, M., and Hu, J.: The role of naphthalene and its derivatives in the formation of secondary organic aerosol in the Yangtze River Delta region, China, Atmos. Chem. Phys., 24, 7467–7479, https://doi.org/10.5194/acp-24-7467-2024, 2024.

Zhang, H., Li, H., Zhang, Y., Wang, X., Bi, F., Meng, L., Li, Y., Zhao, L., Zhang, X., Peng, Z., Mu, Y., Mellouki, W., and Chai, F.: Synergistic generation mechanisms of SOA and ozone from the photochemical oxidation of 1,3,5-trimethylbenzene: Influence of precursors ratio, temperature and radiation intensity, Atmos. Res., 293, 106924, https://doi.org/10.1016/j.atmosres.2023.106924, 2023.

Zhang, J., Choi, M., Ji, Y., Zhang, R., Zhang, R., and Ying, Q.: Assessing the Uncertainties in Ozone and SOA Predictions due to Different Branching Ratios of the Cresol Pathway in the Toluene-OH Oxidation Mechanism, ACS Earth Space Chem., 5, 1958–1970, https://doi.org/10.1021/acsearthspacechem.1c00092, 2021.

Zhang, P., Huang, J., Shu, J., and Yang, B.: Comparison of secondary organic aerosol (SOA) formation during *o*-, *m*-, and *p*-xylene photooxidation, Environ. Pollut., 245, 20–28, https://doi.org/10.1016/j.envpol.2018.10.118, 2019a.

Zhang, Q., Xu, Y., and Jia, L.: Secondary organic aerosol formation from OH-initiated oxidation of *m*-xylene: effects of relative humidity on yield and chemical composition, Atmos. Chem. Phys., 19, 15007–15021, https://doi.org/10.5194/acp-19-15007-2019, 2019b.

Zhao, D., Schmitt, S. H., Wang, M., Acir, I.-H., Tillmann, R., Tan, Z., Novelli, A., Fuchs, H., Pullinen, I., Wegener, R., Rohrer, F., Wildt, J., Kiendler-Scharr, A., Wahner, A., and Mentel, T. F.: Effects of NO_x and SO_2 on the secondary organic aerosol formation from photooxidation of α-pinene and limonene, Atmos. Chem. Phys., 18, 1611–1628, https://doi.org/10.5194/acp-18-1611-2018, 2018.

Zhao, J., Zhang, R., Misawa, K., and Shibuya, K.: Experimental product study of the OH-initiated oxidation of *m*-xylene, J. Photoch. Photobio. A, 176, 199–207, https://doi.org/10.1016/j.jphotochem.2005.07.013, 2005.

Zhou, X.: The gas/particle partitioning behavior of phthalate esters in indoor environment: Effects of temperature and humidity, Environ. Res., 194, 110681, https://doi.org/10.1016/j.envres.2020.110681, 2021.

Zhu, M., Huang, M., Xue, B., Cai, S., Hu, C., Zhao, W., Gu, X., and Zhang, W.: Chemical analysis of nitro-aromatic compounds of secondary organic aerosol formed from photooxidation of *p*-xylene with NO_x, J. Chin. Chem. Soc-Taip., 68, 1697–1708, https://doi.org/10.1002/jccs.202100105, 2021.